

# Digital cameras with designs inspired by the arthropod eye

Young Min Song<sup>1\*</sup>, Yizhu Xie<sup>1\*</sup>, Viktor Malyarchuk<sup>1\*</sup>, Jianliang Xiao<sup>2\*</sup>, Inhwa Jung<sup>3</sup>, Ki-Joong Choi<sup>4</sup>, Zhuangjian Liu<sup>5</sup>, Hyunsung Park<sup>6</sup>, Chaofeng Lu<sup>7,8</sup>, Rak-Hwan Kim<sup>1</sup>, Rui Li<sup>8,9</sup>, Kenneth B. Crozier<sup>6</sup>, Yonggang Huang<sup>8</sup> & John A. Rogers<sup>1,4</sup>

**In arthropods, evolution has created a remarkably sophisticated class of imaging systems, with a wide-angle field of view, low aberrations, high acuity to motion and an infinite depth of field<sup>1–3</sup>. A challenge in building digital cameras with the hemispherical, compound apposition layouts of arthropod eyes is that essential design requirements cannot be met with existing planar sensor technologies or conventional optics. Here we present materials, mechanics and integration schemes that afford scalable pathways to working, arthropod-inspired cameras with nearly full hemispherical shapes (about 160 degrees). Their surfaces are densely populated by imaging elements (artificial ommatidia), which are comparable in number (180) to those of the eyes of fire ants (*Solenopsis fugax*) and bark beetles<sup>4,5</sup> (*Hylastes nigrinus*). The devices combine elastomeric compound optical elements with deformable arrays of thin silicon photodetectors into integrated sheets that can be elastically transformed from the planar geometries in which they are fabricated to hemispherical shapes for integration into apposition cameras. Our imaging results and quantitative ray-tracing-based simulations illustrate key features of operation. These general strategies seem to be applicable to other compound eye devices, such as those inspired by moths and lacewings<sup>6,7</sup> (refracting superposition eyes), lobster and shrimp<sup>8</sup> (reflecting superposition eyes), and houseflies<sup>9</sup> (neural superposition eyes).**

Improved understanding of light-sensing organs in biology<sup>1,10–12</sup> creates opportunities for the development of cameras that adopt similar engineering principles, to provide operational characteristics beyond those available with existing technologies<sup>13–19</sup>. The compound eyes of arthropods are particularly notable for their exceptionally wide fields of view, high sensitivity to motion and infinite depth of field<sup>1–3</sup>. Analogous man-made cameras with these characteristics have been of long-standing interest, owing to their potential for use in surveillance devices, tools for endoscopy and other demanding applications. Previous work demonstrates devices that incorporate compound lens systems, but only in planar geometries or in large-scale, handmade curved replicas<sup>20–24</sup>. Constraints intrinsic to such approaches prevent the realization of cameras with the key features present in arthropod eyes: full hemispherical shapes in compact, monolithic forms, with scalability in size, number and configuration of the light-sensing elements (ommatidia).

Here we present a complete set of materials, design layouts and integration schemes for digital cameras that mimic hemispherical apposition compound eyes found in biology. Certain of the concepts extend recent advances in stretchable electronics<sup>25</sup> and hemispherical photodetector arrays<sup>13–18</sup>, in overall strategies that provide previously unachievable options in design. Systematic experimental and theoretical studies of the mechanical and optical properties of working devices reveal the essential aspects of fabrication and operation.

Figure 1a presents schematic illustrations of the two main subsystems and methods for their assembly into working hemispherical apposition cameras. The first subsystem provides optical imaging function and defines the overall mechanics; it is a moulded piece of the elastomer poly(dimethylsiloxane) (PDMS, with index of refraction  $n \approx 1.43$ ) that consists of an array of  $16 \times 16$  convex microlenses (with radius of curvature of each microlens  $r \approx 400 \mu\text{m}$ ) over a square area of  $14.72 \text{ mm} \times 14.72 \text{ mm}$ , as shown in Supplementary Fig. 1. Of the 256 microlenses, 180 form working components of the camera, each on a matching cylindrical supporting post (of height  $h \approx 400 \mu\text{m}$ ) connected to a base membrane (of thickness  $t \approx 550 \mu\text{m}$ ).

The second subsystem enables photodetection and electrical read-out; it consists of a matching array of thin, silicon photodiodes (active areas  $d^2 \approx 160 \mu\text{m} \times 160 \mu\text{m}$ ) and blocking diodes in an open mesh configuration with capability for matrix addressing. Narrow filamentary serpentine traces of metal (Cr/Au) encapsulated by polyimide serve as electrical and mechanical interconnects. Aligned bonding of these two subsystems places each photodiode at the focal position of a corresponding microlens (Fig. 1b), to yield an integrated imaging system. A key feature enabled by the constituent materials and layouts is a fully isotropic elastic mechanical response to large strain deformation, in any direction. In consequence, hydraulic actuation can deterministically transform the planar layout in which these separate subsystems are constructed and bonded together, into a full hemispherical shape (Fig. 1c), with precise engineering control (radius of curvature of the hemisphere  $R \approx 6.96 \text{ mm}$ ) and without any change in optical alignment or adverse effect on electrical or optical performance (see Supplementary Figs 2 and 3 for details).

A complete apposition camera (Fig. 1d) consists of this type of imager, combined with a top perforated sheet and a bottom bulk support, both made of black silicone to eliminate stray light, bonded to the outer and inner surfaces, respectively (Fig. 1e and Supplementary Fig. 8). A thin film insert with metallized contact pads connects to a printed circuit board as an interface to external control electronics.

By analogy to imaging organs in arthropods<sup>12</sup>, each microlens and supporting post corresponds to a corneal lens and crystalline cone, respectively; each photodiode is a rhabdom; the black elastomer serves as the screening pigment. A collected set of each of these elements represents an ommatidium.

The dimensions and the mechanical properties of the imaging system are critically important for proper operation. The acceptance angle ( $\Delta\phi$ ) and the inter-ommatidial angle ( $\Delta\Phi$ ) define the nature of image formation<sup>1,26</sup> (Fig. 1a and Supplementary Fig. 4). Each microlens focuses light incident on it within a cone defined by  $\Delta\phi$ . An individual ommatidium samples an angular object space determined by  $\Delta\Phi$ . For the layouts of Fig. 1a, optical simulation suggests a total field of view of

<sup>1</sup>Department of Materials Science and Engineering, Beckman Institute for Advanced Science and Technology, and Frederick Seitz Materials Research Laboratory, University of Illinois at Urbana-Champaign, Urbana, Illinois 61801, USA. <sup>2</sup>Department of Mechanical Engineering, University of Colorado at Boulder, Boulder, Colorado 80309, USA. <sup>3</sup>Department of Mechanical Engineering, Kyung Hee University, Yongin-si, Gyeonggi-do 446-701, South Korea. <sup>4</sup>Department of Chemistry, University of Illinois at Urbana-Champaign, Urbana, Illinois 61801, USA. <sup>5</sup>Institute of High Performance Computing, A\*star, 1 Fusionopolis Way, #16-16 Connexis 138632, Singapore. <sup>6</sup>School of Engineering and Applied Sciences, Harvard University, Cambridge, Massachusetts 02138, USA. <sup>7</sup>Department of Civil Engineering and Soft Matter Research Center, Zhejiang University, Hangzhou 310058, China. <sup>8</sup>Department of Mechanical Engineering, Department of Civil and Environmental Engineering, Northwestern University, Evanston, Illinois 60208, USA. <sup>9</sup>State Key Laboratory of Structural Analysis for Industrial Equipment, Department of Engineering Mechanics, Dalian University of Technology, Dalian 116024, China.

\*These authors contributed equally to this work.

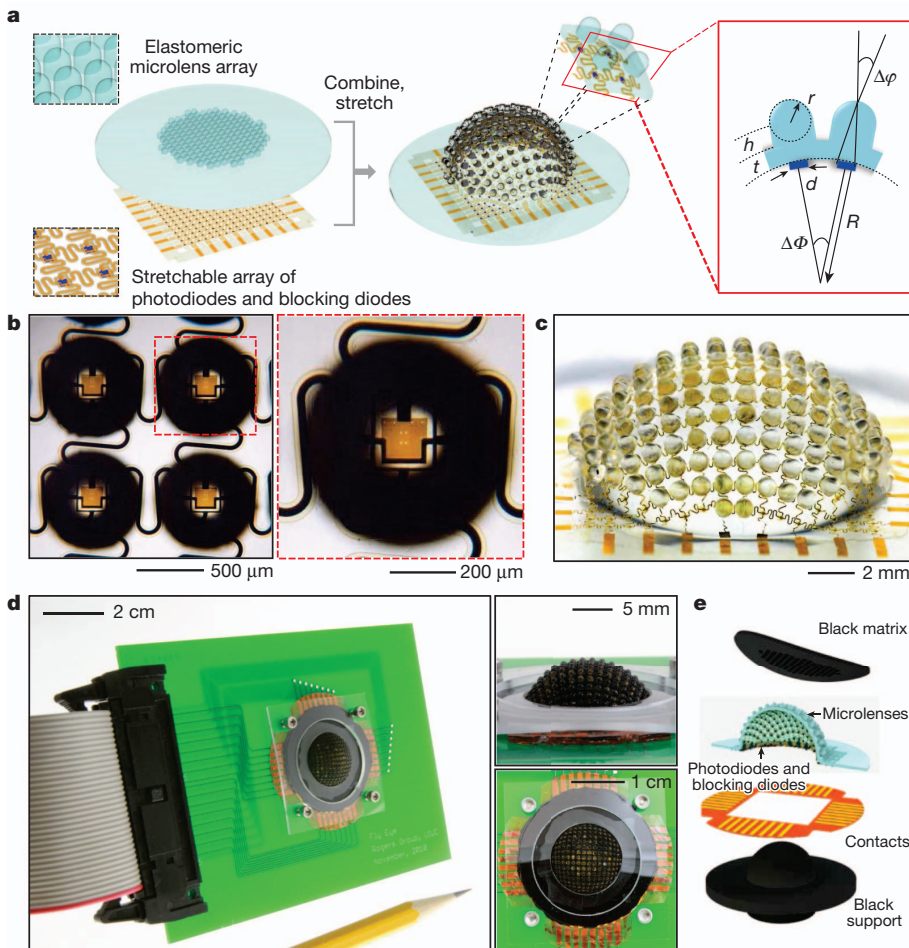


**Figure 1 | Schematic illustrations and images of components and integration schemes for a digital camera that takes the form of a hemispherical, apposition compound eye.**

**a**, Illustrations of an array of elastomeric microlenses and supporting posts joined by a base membrane (above) and a corresponding collection of silicon photodiodes and blocking diodes interconnected by filamentary serpentine wires and configured for matrix addressing (below). On the left, these components are shown in their as-fabricated, planar geometries; the upper and lower insets provide magnified views of four adjacent unit cells (that is, artificial ommatidia). Bonding these two elements and elastically deforming them ('combine, stretch') into a hemispherical shape creates the digital imaging component of an apposition compound eye camera (centre). An exploded view of four adjacent unit cells appears in the centre inset, with a cross-sectional illustration (on the right) that highlights key parameters: the acceptance angle ( $\Delta\phi$ ) for each ommatidium, the inter-ommatidial angle ( $\Delta\Phi$ ), the radius of curvature of the entire device ( $R$ ) and of an individual microlens ( $r$ ), the height of a cylindrical supporting post ( $h$ ), the thickness of the base membrane ( $t$ ), and the diameter of the active area of a photodiode ( $d$ ). **b**, Optical micrograph of four adjacent ommatidia in planar format (left), with magnified view (right). **c**, Image of a representative system after hemispherical deformation. **d**, Photograph of a completed camera mounted on a printed circuit board as an interface to external control electronics (left), with close-ups in the insets (upper inset shows tilted view; lower inset shows top view). **e**, Exploded-view illustration of the components of this system: perforated sheet of black silicone (black matrix), hemispherical array of microlenses and photodiodes/blocking diodes, thin-film contacts for external interconnects, and hemispherical supporting substrate of black silicone.

about  $160^\circ$  when  $\Delta\phi = 9.7^\circ$  and  $\Delta\Phi = 11.0^\circ$ , without overlapping fields in adjacent ommatidia (that is,  $\Delta\phi < \Delta\Phi$ ; see Supplementary Figs 5 and 6 for details). The key dimensions of the optical subsystem— $d$ ,  $r$  and  $h$ —provide these features when implemented with PDMS as the optical material (Supplementary Fig. 7). The combined heights of the microlenses, supporting posts and base membrane (that is,  $r + h + t$ ) position the photodiodes at distances of one focal length ( $f = rn/(n - 1) = r + h + t$ ) from the lens surface. Collimated light at normal incidence focuses to spot sizes that are smaller (about  $100 \mu\text{m} \times 100 \mu\text{m}$ ) than the areas of the photodiodes.

Retaining these optical parameters throughout the process of transformation from planar to hemispherical shapes represents a challenge that can be addressed with two new design/integration approaches. The first approach involves a method for bonding the optical and electrical subsystems at the positions of the photodiodes/blocking diodes only. This configuration ensures optical alignment during subsequent deformation, but allows free motion of the serpentine interconnects to minimize their effects on the overall mechanics. The resulting response of the system to applied force is dominated by the elastic behaviour of the PDMS (modulus about 1 MPa), and is nearly independent of the hard materials found in the array of photodiodes/blocking diodes (Si, with modulus about 150 GPa, Au, with modulus about 80 GPa and polyimide, with modulus about 5 GPa)<sup>27,28</sup>. In particular, the computed effective modulus of the system is only 1.9 MPa, with global strains that can reach more than 50% in equi-biaxial tension before exceeding the fracture thresholds of the materials.

The second approach exploits a set of dimensional and material choices in the optical subsystem. Here, the modulus of the PDMS is sufficiently small and the heights of the supporting posts are sufficiently

large that deformations induced by stretching the base membrane are almost entirely mechanically decoupled from the microlenses. As a result, large strains created by geometry transformation induce no measurable change in the focusing properties. In addition, the combined heights of the microlenses and the posts are large compared to the thickness of the base membrane. This layout minimizes strain at the locations of bonding with the photodiodes/blocking diodes, thereby eliminating the possibility for failure at these interfaces or in the silicon.

Figure 2 summarizes these features in a series of micro X-ray computed tomography (XCT; MicroXCT 400) images and finite element method (FEM) calculations before and after geometrical transformation (see Supplementary Figs 9 and 10 for additional details of FEM and analytical treatments of the mechanics). The results in Fig. 2c highlight four adjacent ommatidia, with strain distributions determined by FEM in each of the different layers of a single ommatidium. The top and bottom surfaces, where the microlenses and photodiodes are located, respectively, show excellent isolation. The peak strains in these regions are  $<1\%$  (microlenses in box of Fig. 2c) and  $<0.2\%$  (photodiode/blocking diodes in box of Fig. 2c) even for the large global strains (about 30% or more) that occur in the hemispherical shape. Quantitative analysis of the distribution of  $r$  across the entire array, before and after deformation (top panels of Fig. 2d; Supplementary Fig. 12) shows no change, which is consistent with FEM findings (Supplementary Fig. 13). Non-uniform strains lead to a slight, but systematic, spatial variation of  $\Delta\Phi$  across the array (bottom left panel of Fig. 2d), as expected based on the mechanics (Supplementary Fig. 13). All ommatidia have an orientation along the direction of the surface normal (that is, the tilt from normal,  $\theta_{\text{tilt}}$ , is zero; bottom right panel of Fig. 2d).

Working apposition cameras formed in this manner have excellent operational characteristics and high yields. Overall image construction follows from a pointwise sampling by the photodiode/blocking diodes of images formed at each microlens. In this way, each ommatidium contributes a single pixel to a different region of the resultant image. Figure 3a schematically illustrates this process through images computed using physically correct ray-tracing procedures (GNU Goptical, see Supplementary Figs 14 and 15 for details) executed in a parallel fashion. Each microlens produces a small image of an object (in this example, a '+' line-art pattern) with a form dictated by the parameters of the lens and the viewing angle (third panel from the left in Fig. 3a). An individual photodiode generates photocurrent only if a portion of the image formed by the associated microlens overlaps the active area. The photodiodes stimulated in this way produce a sampled image (second panel from the left in Fig. 3a) of the object. In biology, rapid motion of the eye and/or the object can yield improvements in effective resolution. Experiments and modelling reported here simulate such effects by scanning the camera from  $-5.5^\circ$  to  $5.5^\circ$  in the  $\theta$  and  $\varphi$  directions with steps of  $1.1^\circ$ . Modelling results appear in the left panel of Fig. 3a (scans from  $-11^\circ$  to  $11^\circ$  lead to complete overlap of contributions from neighbouring ommatidia, thereby allowing subtraction of effects of isolated non-functional elements). Figure 3b presents pictures, rendered on hemispherical surfaces with sizes that match the camera, of two different line-art patterns collected using a representative device, for which 166 out of a total of 180 ommatidia function properly (see Supplementary Fig. 16).

Software algorithms and data acquisition systems enable the cameras to adapt to different light levels. When we use a scanning mode for data collection (see Supplementary Information), the results are remarkably consistent with optical modelling that assumes ideal characteristics for the cameras (Fig. 3c). Systematic, quantitative comparisons

between parametric simulations and experimentally recorded images indicate correlation values (91.3% and 89.0% in left and right images, respectively) in a range consistent with operation close to limits dictated by the optics and physical designs. Some loss of resolution and edge definition follows from parasitic scattering within the camera. See Supplementary Figs 18 and 19 for details. Other examples appear in Supplementary Fig. 20.

The arthropod eye offers resolution determined by the numbers of ommatidia, and is typically modest (Fig. 3b and c) compared, for example, to mammalian eyes. Two other attributes, however, provide powerful modes of perception. First, the hemispherical apposition design enables exceptionally wide-angle fields of view, without off-axis aberrations. Figure 4a gives an example of this characteristic, through pictures of a line-art soccer ball illustration placed at three different angular positions:  $-50^\circ$  (left),  $0^\circ$  (centre), and  $50^\circ$  (right). All three cases show comparable clarity, without anomalous blurring or aberrations, consistent with the proper, independent functioning of ommatidia to obtain using planar detector technologies even with sophisticated fish-eye lenses, spherical mirrors or other specialized optics. Quantitative analysis can be performed through laser illumination at angles ranging from  $-80^\circ$  to  $80^\circ$  with  $20^\circ$  steps along both the  $x$  and  $y$  directions, as shown in a single composite image in Fig. 4b (see individual images in Supplementary Fig. 21). The uniformity in sizes, shapes, illumination levels and positions of these spots are consistent with expected behaviour over the entire approximately  $160^\circ$  field of view.

The second attribute is the nearly infinite depth of field that results from the short focal length of each microlens and the nature of image formation<sup>3</sup>. In particular, as an object moves away from the camera, the size of the image decreases but remains in focus (Supplementary Fig. 22). A consequence is that the camera can accurately and

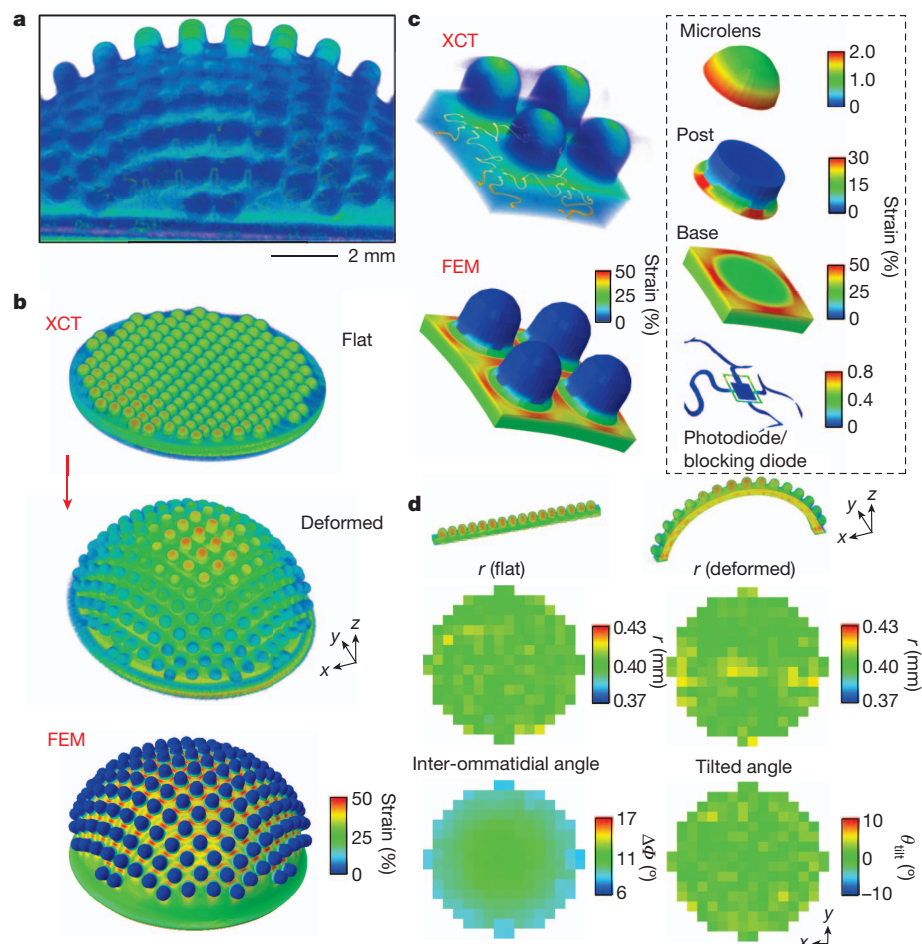


**Figure 2 | Computational and experimental studies of the mechanics associated with assembly of a hemispherical, apposition compound eye camera.** **a**, XCT image of the imaging component of the camera, showing both the microlenses and the photodiodes/blocking diodes with serpentine interconnects (see Supplementary Fig. 11 for additional details of XCT). **b**, XCT images before (top) and after (middle) elastic deformation into a hemispherical shape, and FEM results for the system after deformation (bottom). **c**, High-resolution XCT image of four adjacent ommatidia located slightly off-axis (in polar and azimuth angles) near the centre of a camera, and FEM computed shape and distributions of strain at this location. The boxed panels highlight strains in different regions of a single ommatidium: microlens, cylindrical post, membrane base and photodiode/blocking diode island with serpentine interconnects. **d**, The top panels are XCT images of 16 microlenses from the middle row of an array in flat (left) and hemispherical (right) geometries. The middle panels are colour maps of the radii of curvature ( $r$ ) of microlenses in the array, in flat (left) and hemispherical deformed (right) geometries. The bottom panels are colour maps of  $\Delta\Phi$  (left) and the angle of tilt of ommatidia away from the surface normal  $\theta_{\text{tilt}}$  (right); both in the hemispherical deformed configuration.

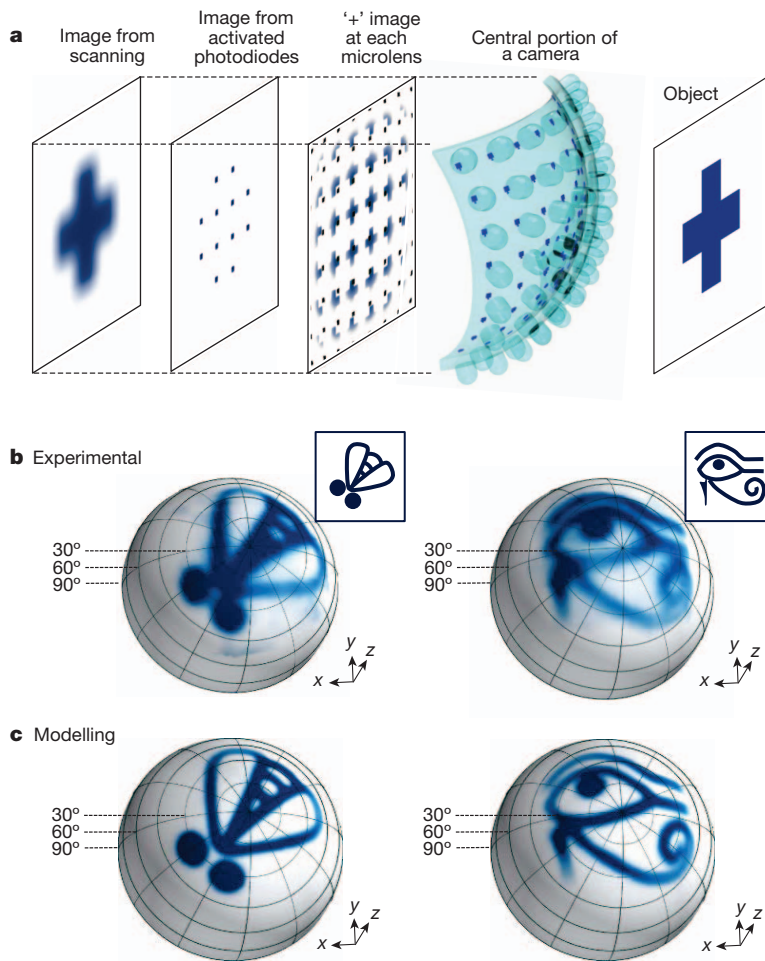


**Figure 3 | Operating principles of a hemispherical, apposition compound eye camera and representative pictures.** **a**, Conceptual view of image formation, illustrated by quantitative ray-tracing results for the simple case of an  $8 \times 8$  hemispherical array of ommatidia, corresponding to the central region of the camera. Each microlens generates an image of the object ('+' pattern in this example), with characteristics determined by the viewing angle. Overlap of a portion of each image with the active area of a corresponding photodiode (black squares in the third frame from left) generates a proportional photocurrent at this location of the array (second frame from left). The result is a sampled reproduction of the object. Improved effective resolution can be realized by scanning the camera (from  $-5.5^\circ$  to  $5.5^\circ$  in the  $\theta$  and  $\phi$  directions with  $1.1^\circ$  steps, as shown in the left frame). **b**, Pictures (main panels) of line-art illustrations of a fly (left inset) and a 'Horus eye' (an Egyptian hieroglyphic character) (right inset) captured with a hemispherical, apposition compound eye camera, each rendered on a hemispherical surface that matches the shape of the device. Experimental setups appear in Supplementary Fig. 17. **c**, Images as in **b**, computed by ray-tracing analysis, assuming ideal construction and operation of the camera.

simultaneously render pictures of multiple objects in a field of view, even at widely different angular positions and distances. Figure 4d presents the results of demonstration experiments. Even though movement of the object away from the camera changes its size in

the corresponding image, the focus is maintained. Objects with the same angular size that are located at different distances produce images with the same size, all of which is consistent with modelling (Supplementary Fig. 23).

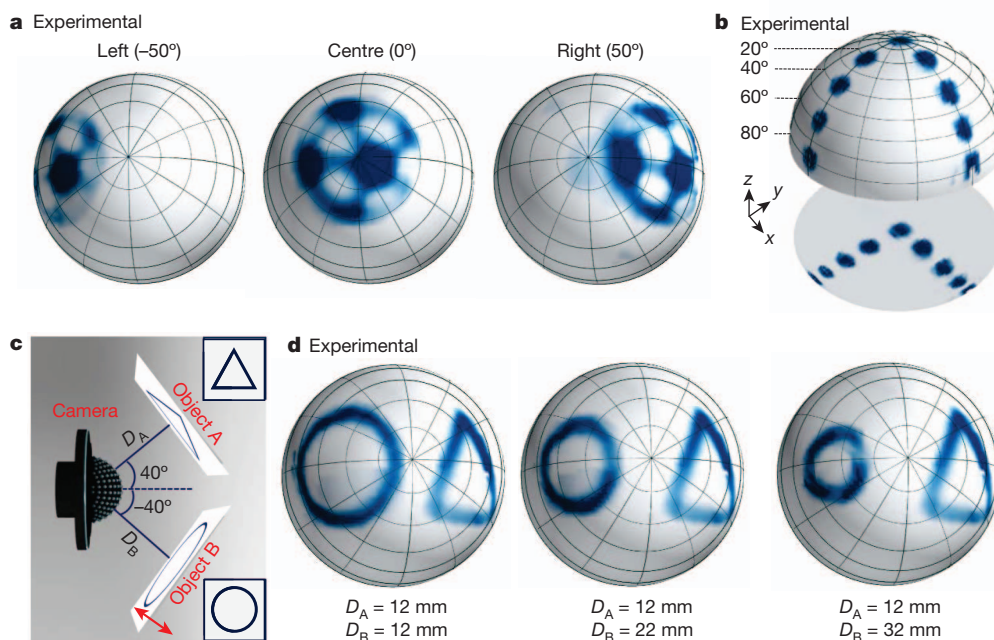


**Figure 4 | Imaging characteristics of a hemispherical, apposition compound eye camera.** **a**, Pictures of a soccer ball illustration captured at three different polar angles relative to the centre of the camera:  $-50^\circ$  (left),  $0^\circ$  (centre), and  $50^\circ$  (right). **b**, Composite picture corresponding to sequential illumination of the camera with a collimated laser beam at nine different angles of incidence (from  $-80^\circ$  to  $80^\circ$  in both  $x$  and  $y$  directions, with  $20^\circ$  steps), displayed on a hemispherical surface (top) and projected onto a plane (bottom). **c**, Schematic illustration of an experimental setup to demonstrate key imaging characteristics. One object (object A, triangle) lies at an angular position of  $40^\circ$  and distance  $D_A$ ; the other (object B, circle) at  $-40^\circ$  and  $D_B$ . **d**, Pictures of these objects collected at different values of  $D_B$ .

The cameras reported here incorporate approximately twice as many ommatidia (about 180) as eyes found in some worker ants (about 100 in *Linepithema humile*)<sup>29</sup>, significantly fewer than in dragonflies (about 28,000 in *Anax junius*)<sup>10</sup> or praying mantises (about 15,000 in *Stagmatoptera biocellata*)<sup>30</sup>, but all with similar fields of view (an estimated 140–180 degrees).

A key defining attribute of our elastomeric optical and deformable electronic subsystems is their applicability to devices with large numbers of ommatidia, diverse spatial layouts, and dimensions into the micrometre regime. Compatibility with silicon technology suggests that commercially available sophistication in imaging arrays and straightforward advances in assembly hardware can enable apposition cameras with resolution and other capabilities that significantly exceed those in known species of arthropods. Specific application requirements and design considerations will dictate the choice between apposition cameras and more conventional approaches that use advanced imaging systems based on fish-eye lenses and others. Other important directions for future research include efforts to expand capabilities beyond those found in biology, such as engineering systems for continuous tuning of the curvature of the hemispherical supporting substrate. Biologically inspired schemes for adapting to different light levels are also of interest.

## METHODS SUMMARY

The optical subsystem was formed by casting and curing a prepolymer to PDMS (Sylgard 184, Dow Corning) against a precision, micro-machined aluminium mould and associated fixture. Release of the cured PDMS yielded microlenses and supporting posts with a thin PDMS membrane as a base, each with well defined dimensions. Fabrication of the electrical subsystem involved a series of thin-film processing steps conducted on a silicon-on-insulator wafer. As a final step, etching with concentrated hydrofluoric acid removed the buried oxide layer. Subsequent transfer printing onto the rear plane of the optical subsystem used a homebuilt apparatus, with integrated microscope stage to enable precise alignment. Irreversible bonding at the positions of the photodiodes/blocking diodes was enabled by layers of SiO<sub>2</sub> deposited only in these regions, to allow condensation reactions between their hydroxyl-terminated surfaces and those of the PDMS. A polyimide film with metal contact pads was mounted onto the periphery of the resulting system with an adhesive. A custom mounting assembly and sealed chamber enabled hydraulic deformation from a planar to hemispherical geometry. A hemispherical supporting rod made of PDMS mixed with black silicone pigment (Smooth-on Inc.), and coated with a thin layer of adhesive, held the system in its deformed, hemispherical geometry. A perforated sheet of black silicone, formed by laser machining of thin film membrane (Ecoflex, Smooth-on) mixed with carbon black powder (Strem Chemical), was manually stretched and assembled onto the imager. Mounting on a printed circuit board using mechanical pressure applied with a plastic frame established good electrical contact between the printed circuit board and the metal contacts on the polyimide film. The completed cameras collected pictures of opaque line-art patterns on transparency foils illuminated from behind with diffuse white light, using automated scanning and data acquisition systems.

Received 21 January; accepted 18 March 2013.

1. Warrant, E. & Nilsson, D.-E. *Invertebrate Vision* Ch. 1 (Cambridge Univ. Press, 2006).
2. Dudley, R. *The Biomechanics of Insect Flight: Form, Function, Evolution* Ch. 5 (Princeton Univ. Press, 2000).
3. Floreano, D., Zufferey, J.-C., Srinivasan, M. V. & Ellington, C. *Flying Insects and Robot* Ch. 10 (Springer, 2009).
4. Wheeler, W. M. *Ants: their Structure, Development and Behavior* Ch. 4 (Columbia Univ. Press, 1910).
5. Chapman, J. A. Ommatidia numbers and eyes in Scolytid beetles. *Ann. Entomol. Soc. Am.* **65**, 550–553 (1972).

6. Horridge, G. A., McLean, M., Stange, G. & Lillywhite, P. G. A diurnal moth superposition eye with high resolution *Phalaenoides tritifica* (Agaristidae). *Proc. R. Soc. Lond. B* **196**, 233–250 (1977).
7. Kral, K. & Stelzl, M. Daily visual sensitivity pattern in the green lacewing *Chrysoperla carnea* (Neuroptera: Chrysopidae). *Eur. J. Entomol.* **95**, 327–333 (1998).
8. Nilsson, D.-E. A new type of imaging optics in compound eyes. *Nature* **332**, 76–78 (1988).
9. Zeil, J. A new kind of neural superposition eye: the compound eye of male Bibionidae. *Nature* **278**, 249–250 (1979).
10. Land, M. F. & Nilsson, D.-E. *Animal Eyes* (Oxford Univ. Press, 2002).
11. Land, M. F. The optics of animal eyes. *Contemp. Phys.* **29**, 435–455 (1988).
12. Nilsson, D.-E. Vision optics and evolution. *Bioscience* **39**, 298–307 (1989).
13. Ko, H. C. *et al.* A hemispherical electronic eye camera based on compressible silicon optoelectronics. *Nature* **454**, 748–753 (2008).
14. Jung, I. *et al.* Dynamically tunable hemispherical electronic eye camera system with adjustable zoom capability. *Proc. Natl Acad. Sci. USA* **108**, 1788–1793 (2011).
15. Hung, P. J., Jeong, K., Liu, G. L. & Lee, L. P. Microfabricated suspensions for electrical connections on the tunable elastomer membrane. *Appl. Phys. Lett.* **85**, 6051–6053 (2004).
16. Jeong, K., Kim, J. & Lee, L. P. Biologically inspired artificial compound eyes. *Science* **312**, 557–561 (2006).
17. Dinyari, R., Rim, S.-B., Huang, K., Catrysse, P. B. & Peumans, P. Curving monolithic silicon for nonplanar focal plane array applications. *Appl. Phys. Lett.* **92**, 191114 (2008).
18. Xu, X., Davanco, M., Qi, X. F. & Forrest, S. R. Direct transfer patterning on three dimensionally deformed surfaces at micrometer resolutions and its application to hemispherical focal plane detector arrays. *Org. Electron.* **9**, 1122–1127 (2008).
19. Street, R. A., Wong, W. S. & Lujan, R. Curved electronic pixel arrays using a cut and bend approach. *J. Appl. Phys.* **105**, 104504 (2009).
20. Tanida, J. *et al.* Thin observation module by bound optics (TOMBO): concept and experimental verification. *Appl. Opt.* **40**, 1806–1813 (2001).
21. Duparré, J., Wippermann, F., Dannberg, P. & Reimann, A. Chirped arrays of refractive ellipsoidal microlenses for aberration correction under oblique incidence. *Opt. Express* **13**, 10539–10551 (2005).
22. Li, L. & Yi, A. Y. Development of a 3D artificial compound eye. *Opt. Express* **18**, 18125–18137 (2010).
23. Franceschini, N., Pichon, J. M. & Blanes, C. From insect vision to robot vision. *Phil. Trans. R. Soc. Lond. B* **337**, 283–294 (1992).
24. Afshari, H. *et al.* The PANOPTIC camera: a plenoptic sensor with real-time omnidirectional capability. *J. Sign. Process Syst.* <http://dx.doi.org/10.1007/s11265-012-0668-4> (2012).
25. Someya, T. *Stretchable Electronics* (Wiley, 2013).
26. Land, M. F. Visual acuity in insects. *Annu. Rev. Entomol.* **42**, 147–177 (1997).
27. Wang, S. *et al.* Mechanics of curvilinear electronics. *Soft Matter* **6**, 5757–5763 (2010).
28. Lu, C. *et al.* Mechanics of tunable hemispherical electronic eye camera systems that combine rigid device elements with soft elastomers. *J. Appl. Mech.* (in the press).
29. Wild, A. L. *Taxonomic Revision of the Ant Genus Linepithema (Hymenoptera: Formicidae)* (Univ. California Press, 2007).
30. Barrós-Pita, J. C. & Maldonado, H. A fovea in the praying mantis eye II. Some morphological characteristics. *Z. Vgl. Physiol.* **67**, 79–92 (1970).

Supplementary Information is available in the online version of the paper.

**Acknowledgements** The work on integration schemes and mechanical designs was supported by the Defense Advanced Research Projects Agency (DARPA) Nanoelectromechanical /Microelectromechanical Science & Technology (N/MEMS S&T) Fundamentals programme under grant number N66001-10-1-4008 issued by the Space and Naval Warfare Systems Center Pacific (SPAWAR). The work on materials, optical modelling and imaging aspects was supported by the National Science Foundation through an Emerging Frontiers in Research and Innovation (EFRI) programme.

**Author Contributions** Y.M.S., Y.X., V.M., J.X. and J.A.R. designed the experiments, Y.M.S., Y.X., V.M., J.X., I.J., K.-J.C., Z.L., H.P., C.L., R.-H.K., R.L., K.B.C., Y.H. and J.A.R. performed the experiments and analysis. Y.M.S., V.M., J.X. and J.A.R. wrote the paper.

**Author Information** Reprints and permissions information is available at [www.nature.com/reprints](http://www.nature.com/reprints). The authors declare no competing financial interests. Readers are welcome to comment on the online version of the paper. Correspondence and requests for materials should be addressed to J.A.R. ([jrogers@illinois.edu](mailto:jrogers@illinois.edu)).

### **1. Fabrication of the photodiode/blocking diode array and its *I-V* characteristics**

Figure S2a shows an exploded schematic illustration of the layout of the silicon, metal and polymer layers associated with a single unit cell in the array. The steps for fabrication generally follow procedures previously reported<sup>1,2</sup>, although the specific designs here were adapted to allow the desired acceptance angle and the extreme requirements on deformability. One major change is the use of second metallization layer to connect the parallel metal lines indirectly passing through the n-type silicon, as shown in Fig. S2a. This modification provides reduced series resistance and prevents line failures that can arise from disconnection between the silicon devices and the metal contacts. Figure S2b presents an image of a 16x16 photodiode/blocking diode array on an SOI wafer before transfer printing. An optical microscope image of the unit cell is in the inset. The response of a representative individual pixel appears in figure S2c. Detailed fabrication steps are outlined in the following.

#### **Fabrication steps:**

##### ***p+* doping**

1. Clean 1.25  $\mu\text{m}$  SOI wafer (acetone, isopropyl alcohol (IPA), deionized (DI) water).
2. Deposit 900 nm  $\text{SiO}_2$  by plasma enhanced chemical vapor deposition (PECVD; PlasmaTherm SLR).
3. Treat with hexamethyldisilazane (HMDS) for 1.5 min.
4. Pattern photoresist (PR; Clariant AZ5214, 3000 rpm, 30 sec) with 365 nm optical lithography (Karl Suss MJB4) (Mask #1: p-doping).
5. Anneal at 110°C for 5 min.
6. Etch oxide in buffered oxide etchant (BOE) for 2.5 min.
7. Remove PR by acetone and clean by piranha for 3 min.
8. Expose to diffusive boron source at 1000°C for 30 min.
9. Clean the processed wafer (HF 1 min, piranha 10 min, BOE 1 min).

##### ***n+* doping**

10. Deposit 900nm  $\text{SiO}_2$  by PECVD.
11. Treat with HMDS for 1.5min.
12. Pattern PR (Mask #2: n-doping).
13. Anneal at 110°C for 5 min.
14. Etch oxide in BOE for 2.5 min.
15. Remove PR by acetone and clean by piranha for 3min.
16. Expose to diffusive phosphorus source at 1000°C for 10min.

17. Clean the processed wafer (HF 1 min, piranha 10 min, BOE 1 min).

#### ***Silicon isolation***

18. Pattern PR (Mask #3: Si isolation).

19. Etch silicon by reactive ion etcher (RIE; 50 mTorr, 40 sccm SF<sub>6</sub>, 100 W, 3 min).

20. Remove PR by acetone and clean by piranha for 3 min.

#### ***Sacrificial oxide layer deposition***

21. Etch oxide layer of SOI wafer in HF for 1.5 min.

22. Deposit 100nm SiO<sub>2</sub> by PECVD.

23. Treat with HMDS for 1.5 min.

24. Pattern PR (Mask #4: sacrificial layer).

25. Anneal at 110°C for 5 min.

26. Etch SiO<sub>2</sub> layer in BOE for 30 sec.

27. Remove PR by acetone and clean by piranha for 3 min.

#### ***Deposition of the first layer of polyimide***

28. Spin coat with polyimide (PI, poly(pyromellitic dianhydride-co-4,4'-oxydianiline), spun at 4000 rpm, 60 sec).

29. Anneal at 110°C for 3 min at 150°C for 10 min.

30. Anneal at 250°C for 60 min in N<sub>2</sub> atmosphere.

#### ***Patterning the first set of via holes***

31. Expose to ultraviolet induced ozone (UVO) for 5 min.

32. Deposit 150 nm SiO<sub>2</sub> by PECVD.

33. Treat with HMDS for 1.5 min.

34. Pattern PR (Mask #5: via pattern 1).

35. Etch SiO<sub>2</sub> layer by RIE (50 mTorr, 40:1.2 sccm CF<sub>4</sub>:O<sub>2</sub>, 150 W, 8.5 min).

36. Remove PR by acetone.

37. Etch PI by RIE (150 mTorr, 20 sccm O<sub>2</sub>, 150 W, 20 min).

#### ***Performing the first metallization***

38. Etch SiO<sub>2</sub> mask in BOE for 35 sec.

39. Sputter 5/300nm of Cr/Au by sputter coater (AJA international).

40. Pattern PR (Mask #6: metal pattern 1).

41. Anneal at 110°C for 5 min.

42. Etch Au/Cr by wet etchants for 80/20 sec.

43. Remove PR by acetone (carefully).

#### ***Depositing the second layer of polyimide***

44. Spin coat with PI (4000 rpm, 60 sec).

45. Anneal at 110°C for 3 min at 150°C for 10 min.

46. Anneal at 250°C for 60 min in N<sub>2</sub> atmosphere.

***Pattern in the second set of via holes***

47. Expose to ultraviolet induced ozone (UVO) for 5 min.

48. Deposit 150 nm SiO<sub>2</sub> by PECVD.

49. Treat with HMDS for 1.5 min.

50. Pattern PR (Mask #7: via pattern 2).

51. Etch SiO<sub>2</sub> layer by RIE (50 mTorr, 40:1.2 sccm CF<sub>4</sub>:O<sub>2</sub>, 150 W, 8.5 min).

52. Remove PR by acetone.

53. Etch PI by RIE (150 mTorr, 20 sccm O<sub>2</sub>, 150 W, 40 min).

***Performing the second metallization***

54. Etch SiO<sub>2</sub> mask in BOE for 35 sec.

55. Sputter 5/300nm of Cr/Au by sputter coater (AJA international).

56. Pattern PR (Mask #8: metal pattern 2).

57. Anneal at 110°C for 5 min.

58. Etch Au/Cr by wet etchants for 80/20 sec.

59. Remove PR by acetone (carefully).

***Depositing the third layer of polyimide***

60. Spin coat with PI (4000 rpm, 60 sec).

61. Anneal at 110°C for 3 min at 150°C for 10 min.

62. Anneal at 250°C for 60 min in N<sub>2</sub> atmosphere.

***Patterning holes and isolating the PI***

63. Expose to ultraviolet induced ozone (UVO) for 5min.

64. Deposit 150 nm SiO<sub>2</sub> by PECVD.

65. Treat with HMDS for 1.5 min.

66. Pattern PR (Mask #9: hole pattern and Mask #10: PI isolation).

67. Etch PECVD oxide by RIE (50 mTorr, 40:1.2 sccm CF<sub>4</sub>:O<sub>2</sub>, 150 W, 8.5 min).

68. Remove PR by acetone.

69. Etch PI by RIE (150 mTorr, 20 sccm O<sub>2</sub>, 150 W, 40 min).

70. Etch Au/Cr by wet etchants for 40/10 sec.

71. Etch PI by RIE (150 mTorr, 20 sccm O<sub>2</sub>, 150 W, 40 min).

72. Etch silicon by RIE (50 mTorr, 40 sccm SF<sub>6</sub>, 100 W, 3 min).

## **2. Method for aligned integration of optical and electrical sub-systems**

Figure S3 illustrates the procedure for aligned integration of the electrical sub-system onto the backside of the optical sub-system. Unlike conventional transfer printing, in this design, the top surface of the device array must bond to the back surfaces of the PDMS microlenses, supporting posts and base membrane. This situation demands a two-step transfer printing scheme, involving 1) transfer of the photodiode/blocking diode arrays from a SOI wafer to a PDMS stamp using a water-soluble poly(vinylalcohol) (PVA) tape, and then 2) aligned transfer from the PDMS stamp to the backside of the PDMS substrate using an assembly of translation and rotation stages with an optical microscope. In the first step, the array was retrieved with water-soluble PVA tape and transferred to a flat PDMS stamp mounted on a glass substrate. After the transfer, the PVA tape was dissolved by immersion in DI water for 30 minutes. In the second step, a thick PDMS supporting substrate with an array of concave recessed regions, in a geometry and layout matching the microlens array, was used as a mount for the PDMS optical sub-system. These two pieces, taken together, were sufficiently rigid to allow use on a mechanical alignment stage. A microscope with a translational/rotational stage enabled alignment, and then controlled bonding of the optical and electrical sub-systems, in a way that matched each photodiode/blocking diode to a microlens. To ensure perfect transfer and robust bonding, the surface of the optical sub-system was treated with ultraviolet induced ozone, to allow adhesion, via condensation reactions, with the photodiodes/blocking diodes upon baking at 70°C. Afterwards, the PDMS stamp was released slowly (~ 10 sec), and the integrated optical/electrical system was removed from the PDMS support. Detailed procedures are as follows.

### **Aligned, transfer printing/bonding of optical and electrical sub-systems**

1. Etch oxide layer of SOI wafer in HF for 60 min.
2. Rinse the processed wafer with DI water for 10 min (carefully).
3. Clean device perimeter using scotch tapes.
4. Pick up photodiode/blocking diode arrays using water-soluble tape.
5. Transfer to a PDMS stamp on a glass substrate.
6. Dissolve the water-soluble tape with DI water for 30 min.
7. Mount PDMS optical sub-system on a thick PDMS support with concave relief in the geometry and layout of the microlens array.
8. Expose PDMS optical sub-system to ultraviolet induced ozone (UVO) for 3 min.

9. Align electrical sub-system mounted on a thin PDMS membrane to optical sub-system.
10. Stamp to a target substrate.
11. Release PDMS stamp (slowly ~ 10sec).
12. Release integrated optical/electrical system from the PDMS supporter.

### **3. Optical design aspects**

Fig. S4 shows a schematic illustration of the compound eye camera before and after deformation, with key optical parameters identified. Each photodiode is positioned at the bottom center of each microlens. Each microlens/photodiode combination (i.e. ommatidium) collects averaged optical signal from light incident within an acceptance angle,  $\Delta\varphi$ , of object space. Before deformation, the distance between microlenses (i.e. the pitch),  $L_0$ , is 0.92 mm. After deformation, the planar layout transforms into a full hemispherical shape, such that the compound eye samples the angular object space with an inter-ommatidial angle,  $\Delta\Phi$ , as shown in the bottom frame of Fig. S4. The spherical radius and the polar angle are

$$R = \frac{H^2 + r_s^2}{2H}, \quad \beta = \sin^{-1} \frac{H}{R} \quad (1)$$

where  $H=6 \text{ mm}$  and  $r_s=6.86 \text{ mm}$  are the height and radius of the spherical cap, respectively.

The tensile stretch is given by  $\rho = \frac{2R\beta}{2r_s}$  and the pitch after deformation is determined by

$L = \rho L_0$ . Then, the inter-ommatidial angle is defined by  $\Delta\Phi = \frac{L}{R}$ . Fig. S5b shows the

relation between the height of the deformed optical/electrical system and the inter-ommatidial angle. For  $H = r_s$ , the spherical cap becomes a full hemisphere of radius  $R = r_s$  and the

polar angle  $\beta = \frac{\pi}{2}$ . For  $H = 6 \text{ mm}$ , the inter-ommatidial angle  $\Delta\Phi = 11.04^\circ$ , and the field of

view angle  $\theta_{FOV} = 160.4^\circ$ .

At an incident wavelength,  $\lambda$ , the acceptance angle of an ommatidium can be described by the formula<sup>3</sup>

$$\Delta\varphi = \sqrt{\left(\frac{\lambda}{D}\right)^2 + \left(\frac{d}{f}\right)^2}$$

where  $\lambda/D$  is the angular sensitivity due to diffraction at a facet lens with diameter  $D$  and  $d/f$  is the angular sensitivity due to the geometrical angle of a photodiode with diameter  $d$

with  $f$  as the focal length of the microlens. In our design, diffraction is negligible since the microlens diameter is much larger than the optical wavelength. As a result, the acceptance angle  $\Delta\varphi$  is simply determined by  $d/f$ . Fig. S5b summarizes focal lengths at different radii of curvature, along with other parameters, evaluated by numerical ray tracing (Optical\_bench)<sup>4</sup>. The parameters of the ommatidia were defined to ensure that the detector is in the focus of the microlens. A range of input angles for the rays that intersect the detector were evaluated and used to guide design process. Since the detector has a square shape, two sets of input angles were considered: those parallel to the side and to the diagonal of the square. In the current design, the radii of curvature should be less than 0.46 mm because the distance between adjacent detectors is 0.92 mm. We selected the curvature to be 0.4 mm with 0.12 mm gaps between adjacent lenses. The corresponding focal length is 1.37 mm. The key dimensions are in Fig. S5b. For simplicity, we set the focal length as 1.35 mm. The height of the cylindrical support the thickness of the base membrane are 0.40 mm and 0.55 mm, respectively.

The optical sub-system was formed in a single step, by casting and curing a prepolymer to a silicone elastomer (10:1 mixture of base and curing agent, Sylgard 184, Dow Corning) against a precisely machined aluminum block mounted on a fixture, as shown in the left frame of Fig. S1. To minimize the strain from heating, the PDMS was cured at room temperature for 48 hours. Release of the cured PDMS completed the fabrication.

The microlenses fabricated in this manner were characterized by measuring the focused spot with different incident angles. A schematic diagram of the experimental setup is shown in Fig. S6a. Laser light (532 nm) was passed through a beam expander (Thorlabs BE15M), and then onto a microlens array directly laminated on a CMOS sensor. Since the sensor was naturally positioned at the focal point of microlens, the focused spot image could be recorded directly. As the lens/sensor was rotated, the position of the focused spot moved in a radial direction. Figure S6b shows calculation and experimental results of the relation between the acceptance and the distance between each spot. To prevent overlapping of light received by adjacent ommatidium in object space, the acceptance angle should be smaller than the inter-ommatidial angle. For this purpose, we selected a photodiode diameter of 160  $\mu\text{m}$ , corresponding to an acceptance angle of  $9.69^\circ$ .

#### **4. Method for hemispherical deformation and completion of the compound eye camera**

Fig. S8a presents an exploded view of schematic illustration of the compound eye camera, consisting of a highly stretchable, perforated black matrix, arrays of deformable, elastomeric microlenses in a hemispherical layout, coupled with arrays of silicon photodiodes/blocking diodes, a polyimide (PI) film with metal electrodes, and a black hemispherical support. Before hemispherical deformation, a PI film in the form of a circular strip with metal contact pads (third frame of Fig. S8c) was mounted on the rear plane of the integrated optical and electrical sub-systems by use of an adhesive. Electrical connection between the device array and the metal lines on the PI film was established with silver epoxy. For deformation, the integrated imager was sealed in a hydraulic fixture that consisted of an upper and lower cover with an opening hole, as shown in the second frame of Fig. S8c. The opening hole controlled the size and shape of deformation. To enable very large deformation from flat to hemisphere, the edge of opening hole was formed with a rounded surface. The assembly was connected to a fluidic chamber with two liquid input/output ports. These ports were used not only for applying pressure but also for releasing air entrapped in the system. The radius of curvature of the deformed hemisphere was controlled by adjusting the pressure inside of the water chamber using a gauge connected through a t-connector. The deformed imager was mounted on a black hemispherical support rod coated with a thin layer of adhesive to retain the hemispherical geometry. This support was made of PDMS with 5 wt% black silicon pigment (Smooth-on Inc., USA), molded using a machined aluminum block.

The black matrix acts as a light blocking baffle between microlenses, to suppress optical crosstalk between neighboring ommatidia. The steps for fabricating this component started with the mixing of an elastomer (Ecoflex 00-10, Smooth-On, USA) with carbon black powder (Strem chemicals, USA) at 0.5 wt% using a centrifugal mixer (Thinky, USA). This liquid was then spin cast on a 4 inch silicon wafer at 300 rpm for 100 seconds. The film was cured at room temperature for 24 hours. The resulting thickness was  $\sim 800$   $\mu\text{m}$ . After curing, the black silicone film was peeled off from the wafer. Holes were machined using a  $\text{CO}_2$  laser cutter (VLS3.50, Universal Laser, USA) with 2.0 lens kit, in a vector cutting mode with resolution of 1000 pulses per inch. The fabricated matrix appears in the top frame of Fig. S8c. The diameter of the holes was 650  $\mu\text{m}$  and the distance between them was 920  $\mu\text{m}$ . This component was manually assembled with deformed apposition compound eye imager.

Fig. S8b gives a schematic illustration of the fully integrated compound eye camera, ready to mount on a printed circuit board (PCB). Mechanical pressure applied using a transparent plastic frame with a large circular aperture enabled successful electrical contact between the PCB and the metal pads on the PI. Fig. S14 shows the current response for all used pixels (i.e., [2, 8, 10, 12, 14, 14, 14, 16, 16, 14, 14, 14, 12, 10, 8, 2] from first to sixteen column line) at an applied bias of 3 V in the bright (top frame) and dark (bottom frame) state. The current response mapping revealed that 14 pixels out of the 180 pixels (92.2% pixel yields) were not working properly. To eliminate the effects of these malfunctioning pixels in captured pictures, we used an overscanning process.

### **5. Mechanics of hemispherical, large strain deformations**

As shown in Fig. S9a, the optical sub-system consists of an array of PDMS microlenses on supporting cylindrical posts, all bonded to a base PDMS membrane. The PDMS Young's modulus,  $E$ , and Poisson's ratio,  $\nu=0.5$ . This sub-system is deformed to hemispherical shape by hydraulic pressure applied on the bottom through a sealed chamber. The opening of this chamber has a radius of  $R_2$  ( $=10.9$  mm), and the deformation is confined by a stiff ring with inner radius  $R_1$  ( $=7.4$  mm), as illustrated in Fig. S9a. The inner edge of the ring is rounded, with radius  $r_0=1$  mm. Water injection into the chamber induces a pressure difference,  $p$ , at the two surfaces that deforms the PDMS into the shape of a hemispherical cap. The deformation detail is illustrated in Fig. S9b and S9c. The part of the PDMS outside of the inner edge of open hole is confined, and remains undeformed. As shown in Fig. S9c, upon deformation, sliding occurs between the inner edges of the stiff ring and the open hole, such that the  $B$  point on the undeformed shape moves to  $B'$  point. The PDMS membrane will contact the rounded inner edge of the stiff ring, with the separation point  $A'$ , which corresponds to point  $A$  on the undeformed shape.

The mechanical response of the sub-system is approximated by a uniform PDMS membrane. As shown in the previous studies, the radial strain is approximately constant across the membrane. For a peak deflection,  $H$ , of the PDMS membrane, the radius of the hemisphere is obtained as  $R = \frac{(R_1 + r_0)^2 + H^2}{2w} - r_0$ , the spherical angle of the hemispherical cap is  $\varphi_m = \arcsin \frac{R_1 + r_0}{R + r_0}$ , and the coordinate of the separation point  $A'$  is determined by the

cylindrical coordinate  $(r, z) = \left[ \frac{R(R_1 + r_0)}{R + r_0}, \frac{Hr_0}{R + r_0} \right]$ .

The radial coordinate of A can be obtained as

$$r_A = \frac{R_2 R \varphi_m}{(R + r_0) \varphi_m + R_2 - R_1 - r_0}.$$

The material point initially at  $(r < r_A, \theta, 0)$  moves to a new point on the hemispherical cap

with a polar angle  $\varphi = \frac{r}{r_A} \varphi_m$ . The corresponding principle stretches are

$$\lambda_1^{\text{cap}} = \frac{R \varphi_m}{r_A}, \quad \lambda_2^{\text{cap}} = \frac{R}{r} \sin\left(\frac{r}{r_A} \varphi_m\right), \quad \lambda_3^{\text{cap}} = \frac{r_A r}{R^2 \varphi_m \sin(r \varphi_m / r_A)}. \quad (1)$$

The radial coordinate of B point is

$$r_B = \frac{R_2 (R + r_0) \varphi_m}{(R + r_0) \varphi_m + R_2 - R_1 - r_0}.$$

The principle stretches in PDMS in contact with the ring ( $r_A \leq r \leq r_B$ ) are

$$\lambda_1^{\text{contact}} = \frac{R \varphi_m}{r_A}, \quad \lambda_2^{\text{contact}} = \frac{R_1 + r_0}{r} \left[ 1 - \sin\left(\frac{R \varphi_m}{r_A} \frac{r_B - r}{r_0}\right) \right], \quad \lambda_3^{\text{contact}} = \frac{1}{\lambda_1^{\text{contact}} \lambda_2^{\text{contact}}}. \quad (2)$$

The principle stretches in the flat part ( $r_B \leq r \leq R_2$ ) are

$$\lambda_1^{\text{flat}} = \frac{R \varphi_m}{r_A}, \quad \lambda_2^{\text{flat}} = \frac{1}{r} \left[ R_2 - \frac{R_2 - r}{R_2 - r_B} (R_2 - R_1 - r_0) \right], \quad \lambda_3^{\text{flat}} = \frac{1}{\lambda_1^{\text{flat}} \lambda_2^{\text{flat}}}. \quad (3)$$

The elastic strain energy based on the Yeoh model is obtained as<sup>5</sup>

$$U_e = 2\pi t \left[ \int_0^{r_A} \sum_{n=1}^3 C_n (I_1^{\text{cap}} - 3)^n r dr + \int_{r_A}^{r_B} \sum_{n=1}^3 C_n (I_1^{\text{contact}} - 3)^n r dr + \int_{r_B}^{R_2} \sum_{n=1}^3 C_n (I_1^{\text{flat}} - 3)^n r dr \right], \quad (4)$$

where  $I_1 = \lambda_1^2 + \lambda_2^2 + \lambda_3^2$  and  $C_n$  are the material constants reported by Jung et al.<sup>2,6</sup>. The work done by the pressure difference  $p$  is

$$W = pV = p \left\{ \frac{\pi R^3 h}{6(R + r_0)^3} \left[ 3(R_1 + r_0)^2 + H^2 \right] + \pi (R_1 + r_0)^2 \frac{Hr_0}{R + r_0} - V_3 \right\}, \quad (5)$$

where  $V_3 = \pi r_0^2 \left\{ (R_1 + r_0) \left( \varphi_m - \frac{1}{2} \sin 2\varphi_m \right) - r_0 \left[ (1 - \cos \varphi_m) - \frac{1}{3} (1 - \cos^3 \varphi_m) \right] \right\}$ , and  $V$  is the

volume enveloped by the deformed membrane and the  $z = 0$  plane.

The principle of minimum potential energy gives

$$p = \frac{\delta U_e}{\delta V} = \frac{\partial U_e / \partial h}{\partial V / \partial h}. \quad (6)$$

This analytically gives the relation between the pressure difference,  $p$ , and peak deflection,  $H$ . The  $w$ - $p$  curve is plotted as red solid line in Fig. S10a, which shows good agreement with FEM and experiment. Figure S10b shows analytical (red solid line) and experimental (black circles) results for the radius of curvature,  $R$ , versus the applied water pressure, which also exhibit good agreement.

### **6. Analysis of key geometries in the compound eye**

Three dimensional geometries of the compound eye camera were determined by micro X-ray tomography (MicroXCT 400, Xradia). Fig. S11a shows the MicroXCT system. The sample was mounted on a rotation stage and exposed to the X-ray beam field. Two different magnifications, i.e., 0.5x and 4x, were used to capture the whole sample and to reveal additional details of specific areas, respectively. During MicroXCT imaging, the sample was scanned using an X-ray source at 40 KeV and 200 uA, and 700 projections were collected as the sample was rotated stepwise over 180 degrees with a 8 second exposure time for each projection. The shadow images were then processed to reconstruct 2D radiographic cross-sectional image stacks by using the TXM Reconstructor software (Xradia). The distances of the sample to the X-ray source and to the detector were 150 mm and 50 mm, respectively. The resulting voxel (volume pixel) size was  $7.46 \mu\text{m}^3$ . The field of view was approximately  $8000 \mu\text{m} \times 8000 \mu\text{m}$ . Afterwards, the reconstructed images were viewed as 3D volume with TXM 3D Viewer (Xradia). Further image processing was performed using the visualization software package (Amira 5.4.2, Visage Imaging) for reconstructing and rendering 3D virtual images of compound eye camera. For quantitative analysis of reconstructed images, 3D metrology software (Geographic Qualify 2012, GeoMagic Inc., USA) was used.

### **7. Hemispherical imaging simulation and image acquisition**

A unique feature of compound apposition imagers is complete optical isolation of each ommatidium, thereby allowing their independent operation. The result is extreme visual acuity. Exploiting the inherent parallel nature of compound system is also a key

feature of effective optical simulations needed to guide engineering design choices. An optical model was constructed on the assumption that the ommatidia differ only by their positions in the camera. A physically correct ray tracing model was first developed to simulate a single ommatidium (GNU Goptical, C++ optical design and simulation library)<sup>7</sup>. Fans of ~350 randomly distributed rays were propagated through the system and intercepted at the detector surface. Origins of the fans are located at a Lambertian surface placed in front of the camera with intensities that correspond to the object located at this surface.

Modeling of the full compound eye model relied on the combination of individual single ommatidium models calculated in parallel fashion. Figure S14 shows a flow chart of the simulation process. The first stage is to build a set of single optical unit models, initialize them with corresponding ommatidium positions, supply the object to image (30×30 mm, png file) and provide scan pass for the camera. The second stage is the simulation run itself. A virtual cluster (180 in total) is allocated for every ommatidium<sup>8</sup>. The number of nodes in each cluster corresponds to number of lines in the object (usually 300). The result of the simulation is the set of files containing rendered information for every ommatidium/object line combination. The last step is the post-processing procedure of compiling a final image from generated data.

Figure S17 demonstrates the optical setup used to image with the apposition compound eye camera. Diffusive light from an array of light emitting diodes (MB-TBL1X1-W-24, Metaphase Technologies, Inc., USA) provides uniform, white illumination of mounted objects, consisting of a transparency mask with various patterns on an opaque background. Unlike single-lens systems (i.e. camera-type eye), the transmitted light is directly collected by each ommatidium of the compound eye camera without any need in external optics. In order to improve the effective resolution, a scanning procedure was employed, in which the camera was rotated from  $-5.5^\circ$  to  $5.5^\circ$  in the azimuthal and polar directions, in  $1.1^\circ$  increments. Photocurrent generated at each detector was recorded at every scanning step. The recorded photocurrents are digitized for image construction. The process was designed such that the photodiodes always stay in detectors sphere of the camera. This allows high resolution image construction on the hemisphere that matches the detector plane. The distribution of ommatidial axis densities across the fields of view of the compound eye is non-uniform. An adequate mapping algorithm was implemented in the image rendering process to compensate for overlapping of the visual fields that can occur

during the scanning procedures as well as to eliminate areas mapped by non-working pixels.

The performance of the camera can be defined by quantitatively comparing experimentally collected images to those generated by simulation. Specifically, we calculated a comprehensive, parametric set of two dimensional cross correlations between experimentally acquired and simulated images. The standard “correlate2d” function from “signal” module of the “Scientific Python” (<http://www.scipy.org/>) was used for this purpose. The maximum of the output array from this module defines the number of similar pixels between the images. Dividing by total number of pixels and multiplying result by 100 defines a correlation percentage.

## References

1. Ko, H. C. et al. A hemispherical electronic eye camera based on compressible silicon optoelectronics. *Nature* **454**, 748-753 (2008).
2. Jung, I. et al. Dynamically tunable hemispherical electronic eye camera system with adjustable zoom capability. *Proc. Natl Acad. Sci. USA* **108**, 1788-1793 (2011).
3. Land, M. F. Visual acuity in insects. *Annu. Rev. Entomol.* **42**, 147-177 (1997).
4. B. Gustavsson, Optical\_bench. <http://www.mathworks.com/matlabcentral/fileexchange/-27412-opticalbench>.
5. Yeoh, O. H. Some forms of the strain-energy function for rubber. *Rubber Chem. Technol.* **66**, 754-771 (1993).
6. Lu, C. et al. Mechanics of tunable hemispherical electronic eye camera systems that combine rigid device elements with soft elastomers. *J Appl. Mech-T. ASME* (unpublished).
7. Becoulet, A. GNU Goptical, <http://www.gnu.org/software/goptical/>.
8. Thain, D., Tannenbaum, T. & Livny, M. Distributed Computing in Practice: The Condor Experience. *Concurr. Comp.-Pract. E.* **17**, 323-356 (2005).

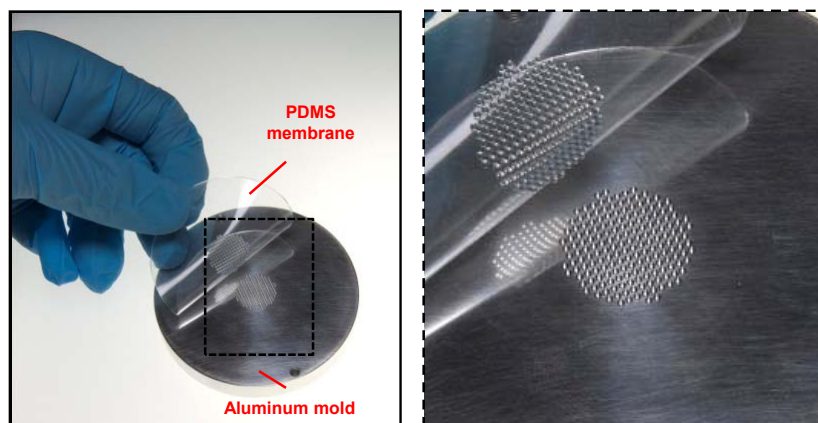


Figure S1. (left) Photograph of precisely machined aluminum block (i.e. mold) with concave-shaped depressions that correspond to arrays of microlenses and cylindrical supporting posts and molded replica in PDMS. (right) Magnified view of left picture.

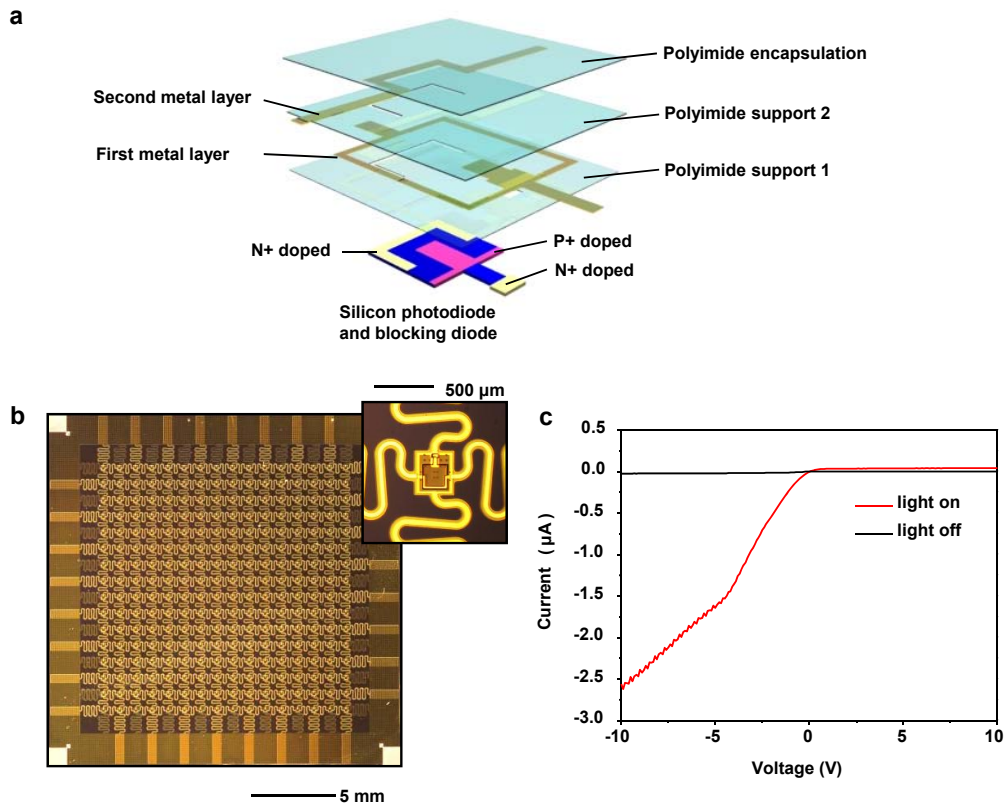


Figure S2. (a) Exploded view schematic illustration of the layout of a silicon photodiode and a blocking diode, along with metal and polymer layers associated with a single unit cell in the array. (b) Photograph of a 16x16 array. (c) I-V curve of a single PD/BD with and without illumination.

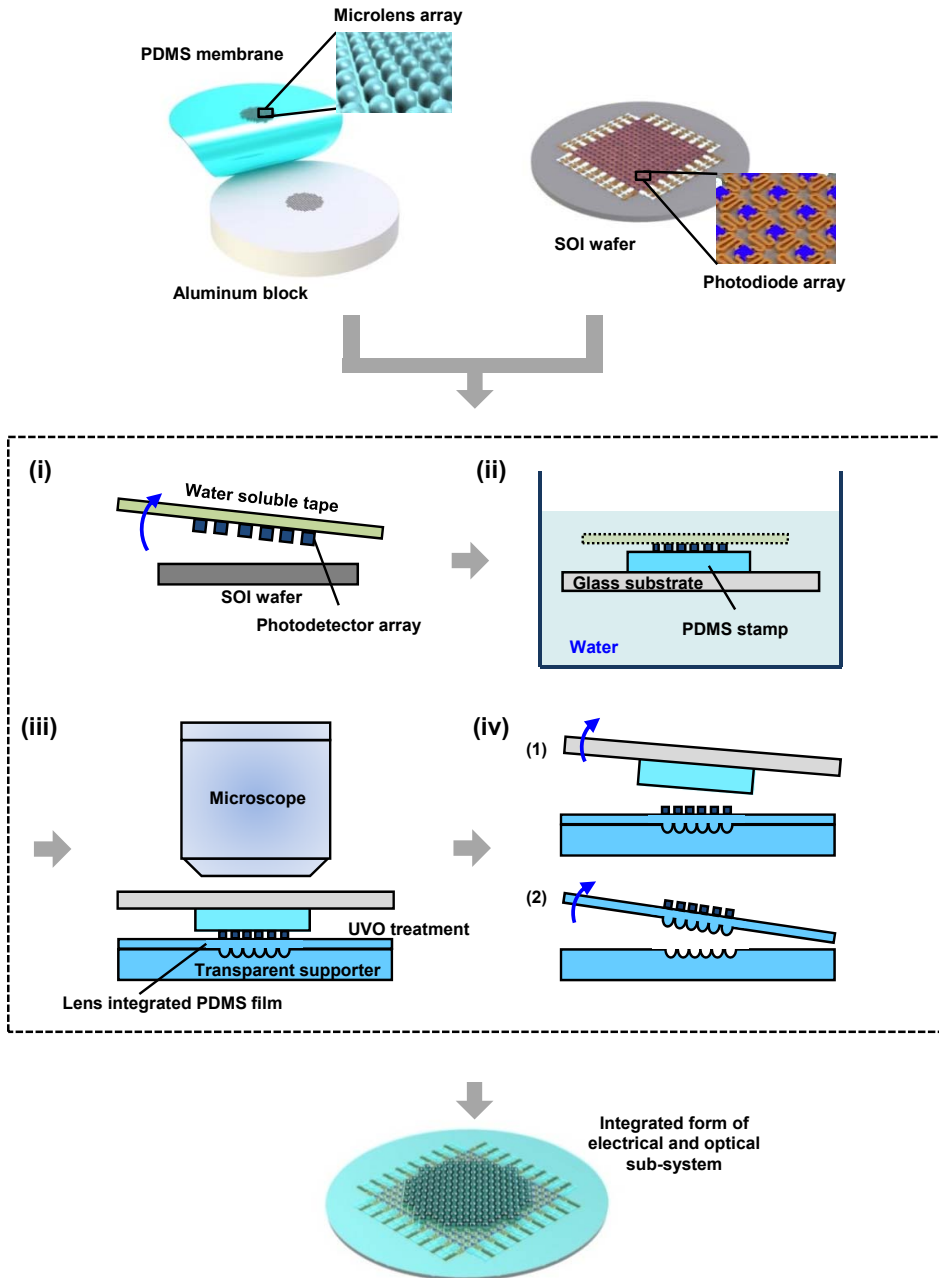


Figure S3. Illustration of steps for transferring and bonding electrical and optical sub-systems.

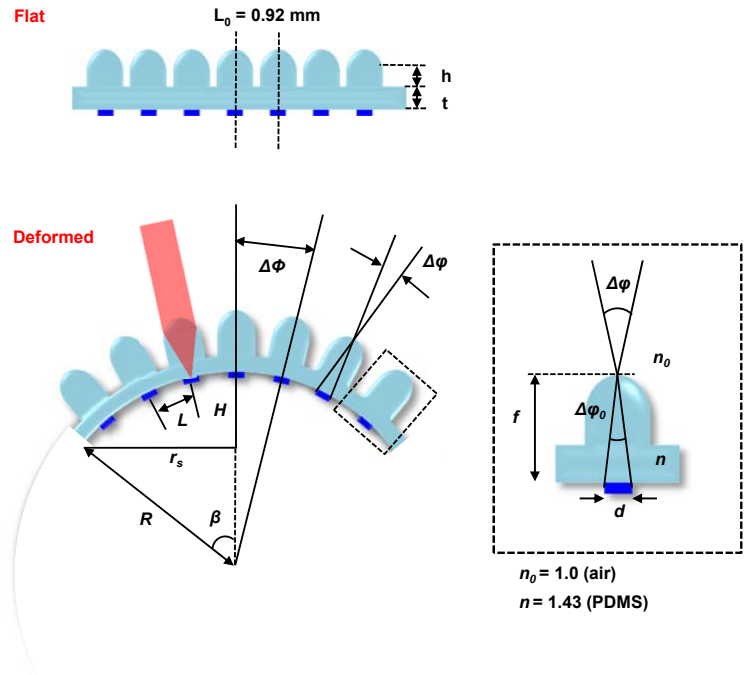


Figure S4. Schematic cross-sectional view of a segment of an apposition eye imager with key parameters in a flat (top) and hemispherical (bottom) shape. The frame on the right provides a detailed view of a single ommatidium.

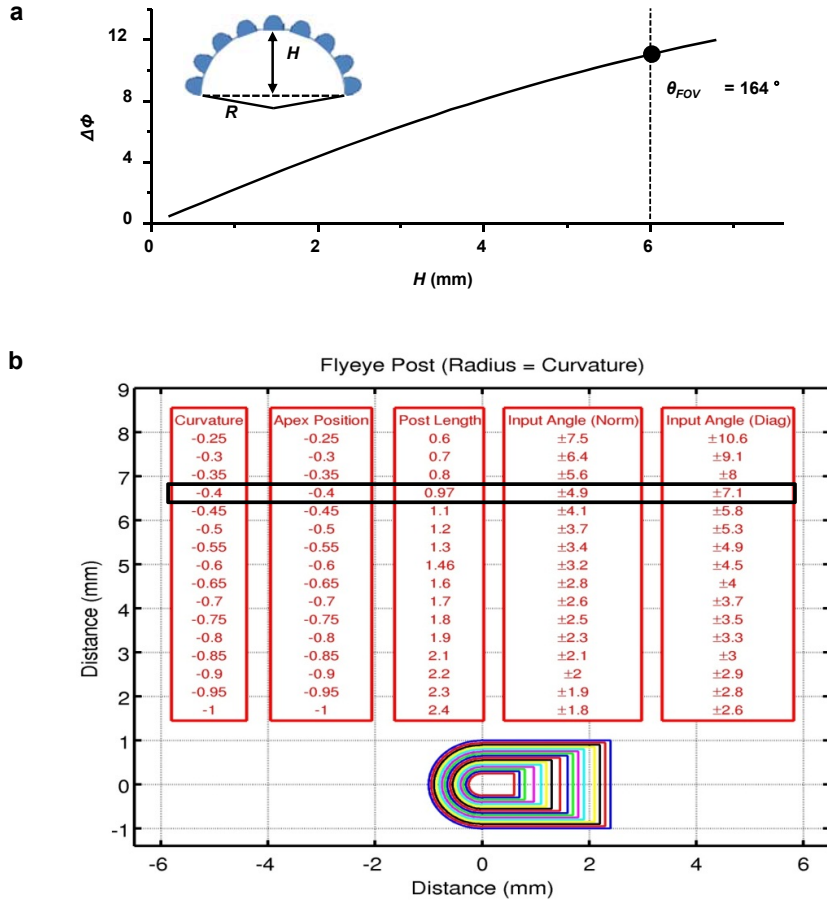


Figure S5. (a) Inter-ommatidial angle as a function of the height of the hemispherical compound eye structure. (b) Determination of microlens parameters via ray tracing calculation.

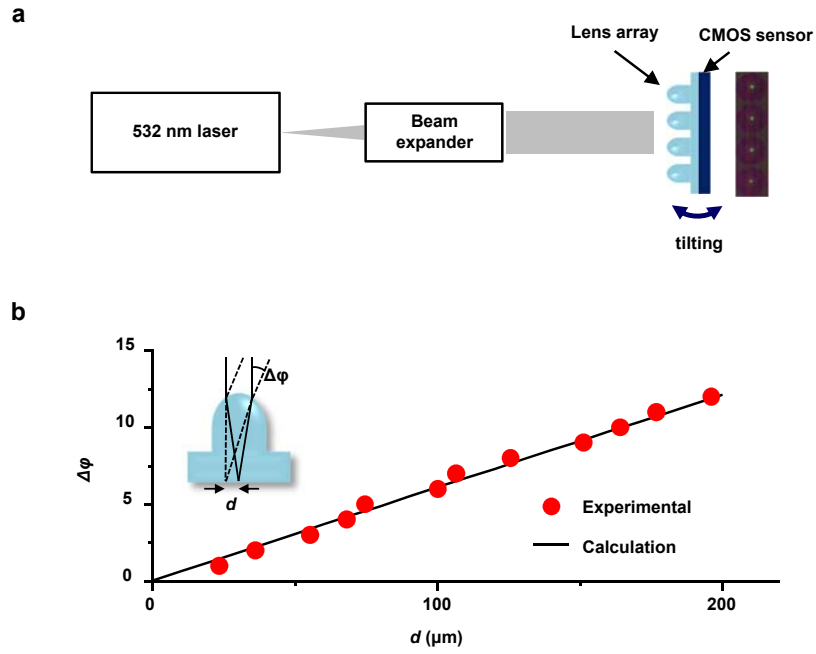


Figure S6. (a) Experimental setup for measurement of acceptance angle. (b) Experimental and calculation results for acceptance angle as a function of diameter of the photodiode.

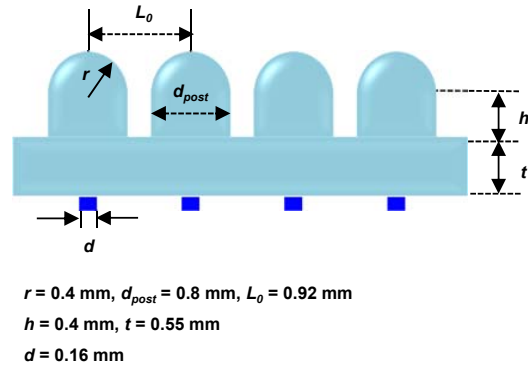


Figure S7. Cross sectional schematic illustration of the layout of four adjacent ommatidia with key dimensions, determined by optical calculation.

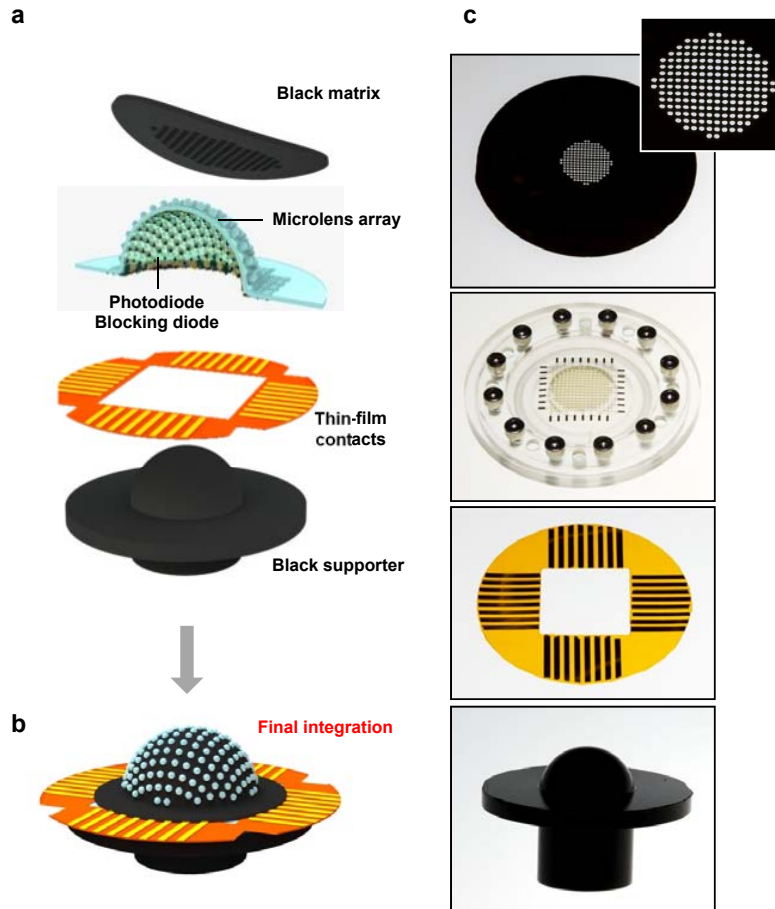


Figure S8. (a) Exploded view illustration of the components of the apposition eye camera: perforated sheet of black PDMS, hemispherical array of microlenses and photodiodes/blocking diodes, thin film pinouts for external interconnects, and a hemispherical supporting substrate of black PDMS (b) Integrated form of the components shown in (a). (c) Images of black matrix (top), microlenses and photodiode/blocking diode arrays with a cover assembly for the hydraulic system (second top), polyimide film with metal electrodes (third top), and black hemispherical support (bottom).

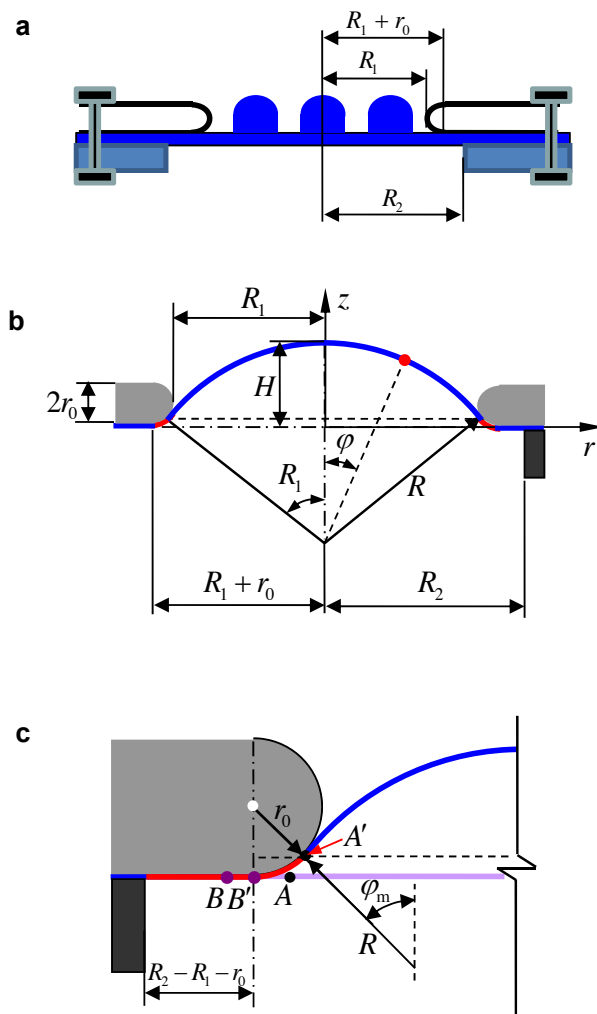


Figure S9. Variable names and geometries corresponding to an analytical model of a PDMS membrane with an array of microlenses, with corresponding key dimensions.

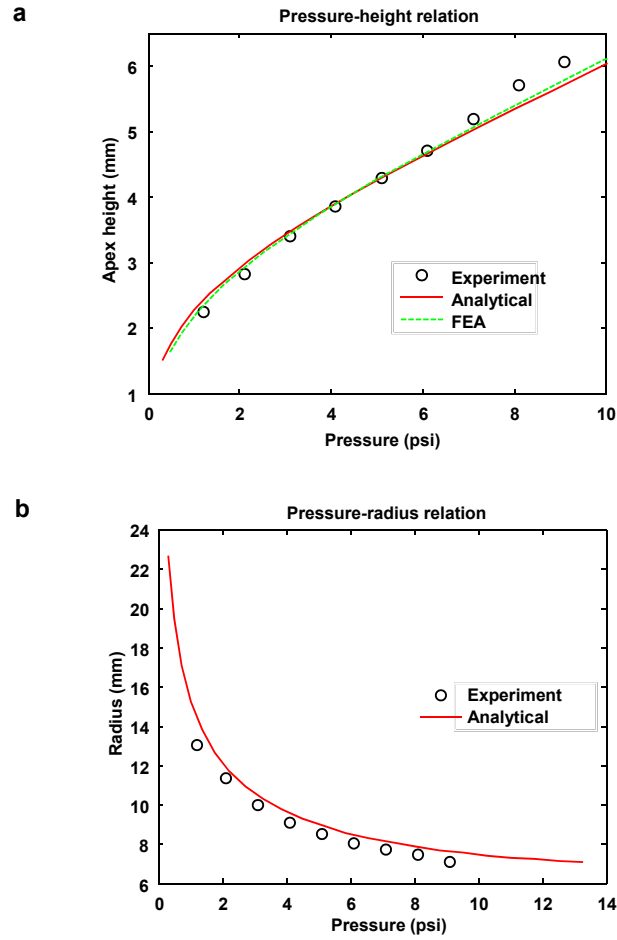


Figure S10. Measurements of (a) height and (b) radius of curvature of the lens surface as a function of applied hydraulic pressure. The results reveal changes that are quantitatively consistent with analytical calculations of the mechanics (analytical; red lines) and finite element analysis (FEA, green line).

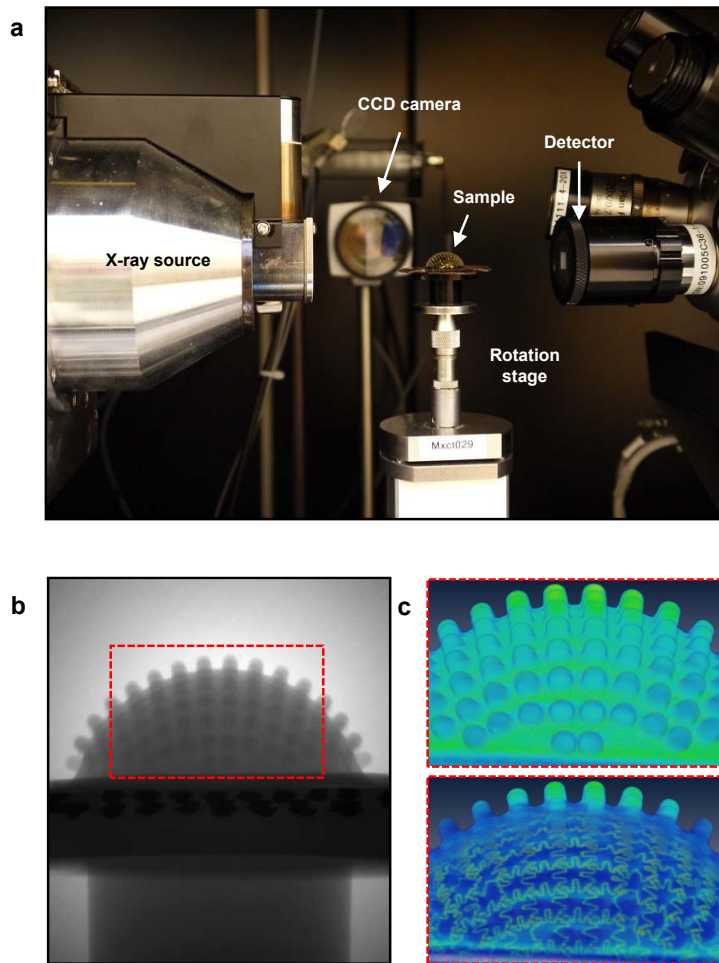


Figure S11. (a) Micro X-ray computed tomography (XCT) system for 3D image acquisition. (b) Radiographic image of the compound eye camera captured by XCT. (c) Reconstructed 3D virtual images. The top and bottom frames correspond to the microlens arrays and the buried metallic interfaces, respectively. In the bottom frame, the microlenses were set to be transparent by adjusting the parameters for color rendering.

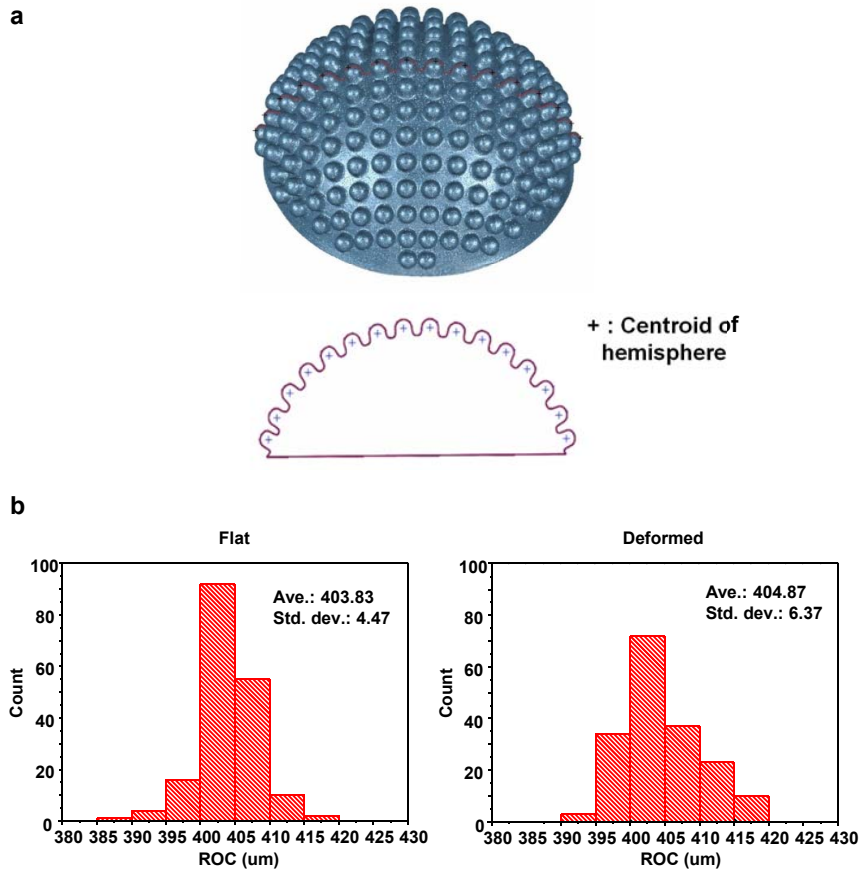


Figure S12. (a) (top) 3D rendered surface of a compound eye imager and (b) cross-sectional image. (b) Histogram of extracted radius of curvature of microlenses for (left) flat and (right) hemispherically deformed geometry.

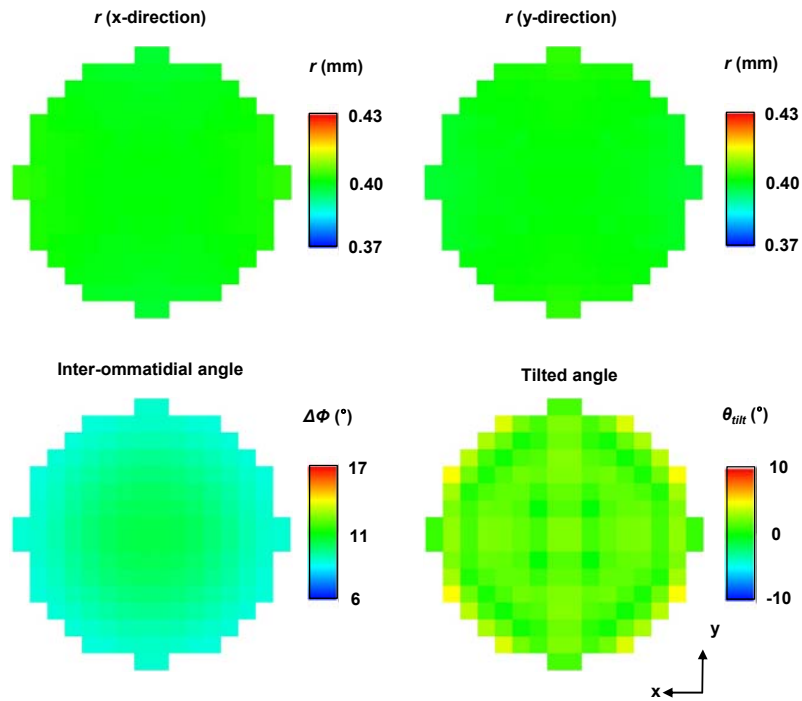


Figure S13. (Top frames) Color maps of FEM simulation results for the radii of curvature ( $r$ ) of microlenses in x- and y-directions (left and right, respectively). (bottom frames) (Bottom frames) Color maps of FEM simulation results for  $\Delta\Phi$  (left) and angles of tilt of ommatidia away from the surface normal ( $\theta_{tilt}$ ; right); All cases correspond to the hemispherical deformed configuration.

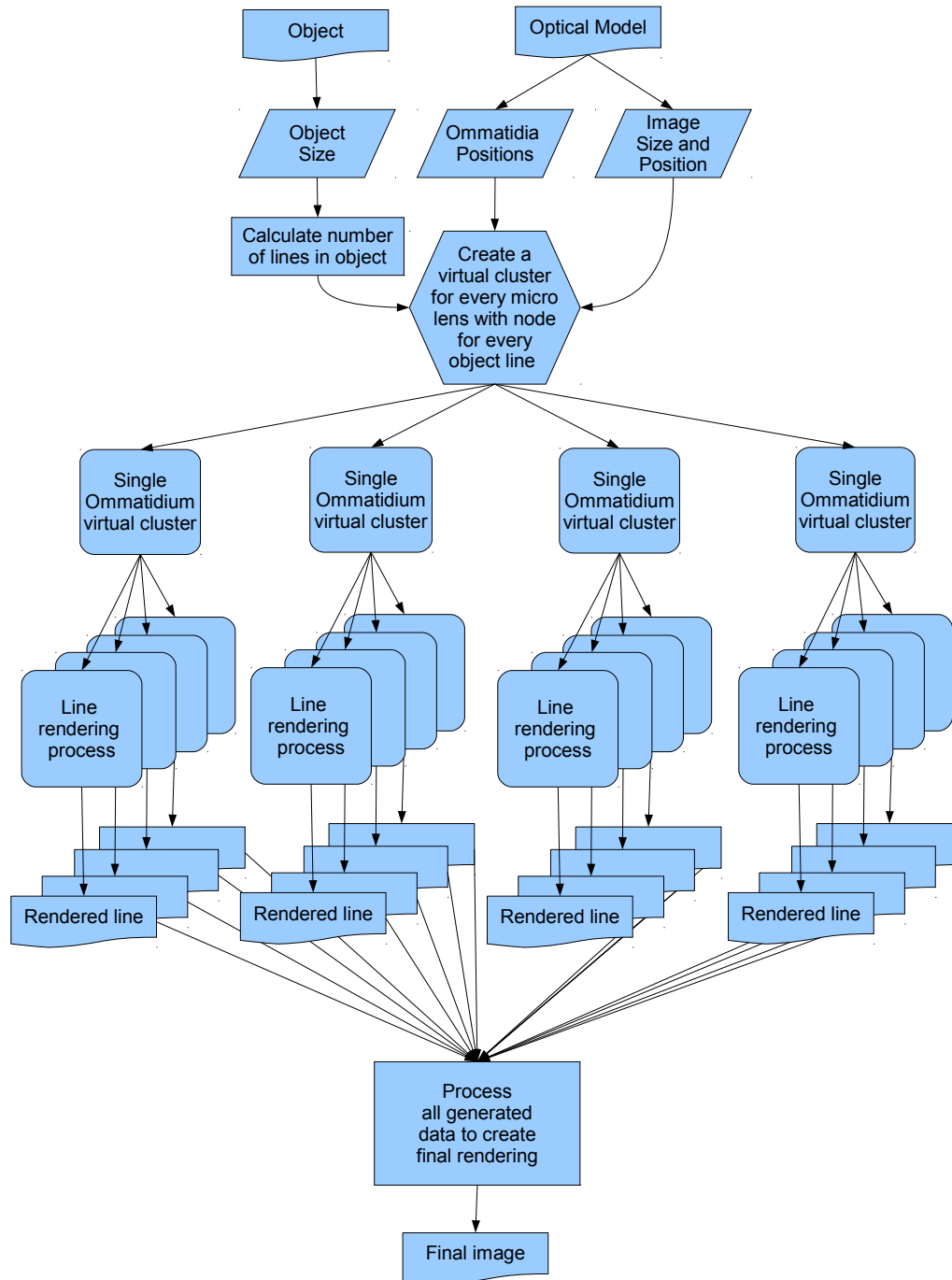


Figure S14. Flowchart for the image simulation process, implemented in a parallel fashion.

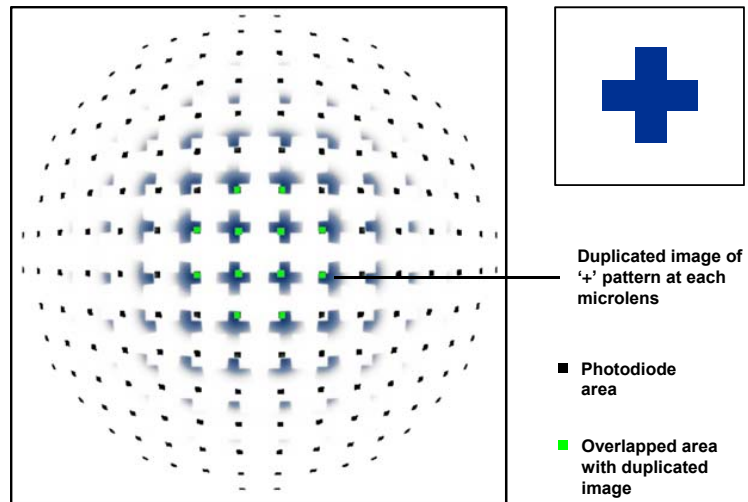


Figure S15. Two-dimensional, overlaid image of duplicated '+' pattern at each microlens on over 180 pixel positions, simulated by ray-tracing. The inset on the right shows the original pattern. The green squares indicate locations where the photodiodes overlap with the duplicated '+' images.

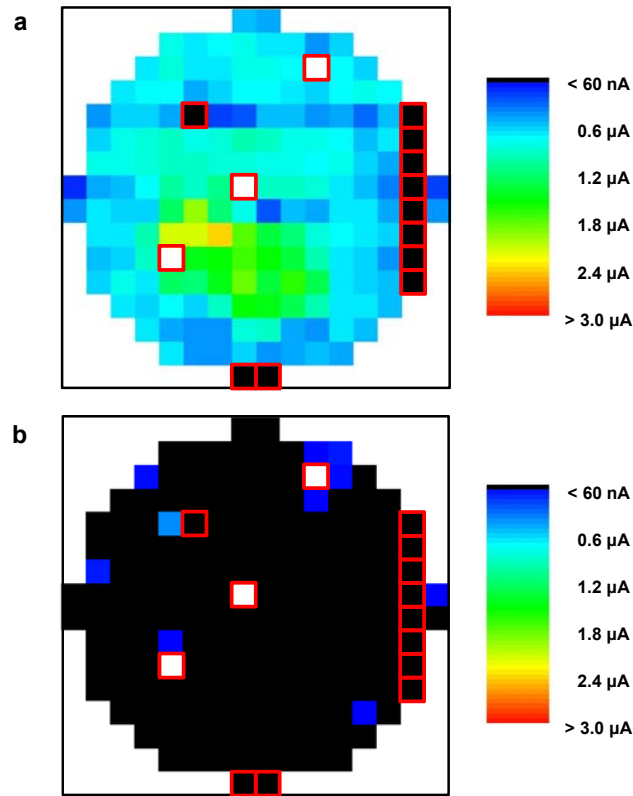


Figure S16. Contour maps of photocurrent recorded from a working camera used in the imaging experiments (a) in a bright light and (b) in a dark environment.

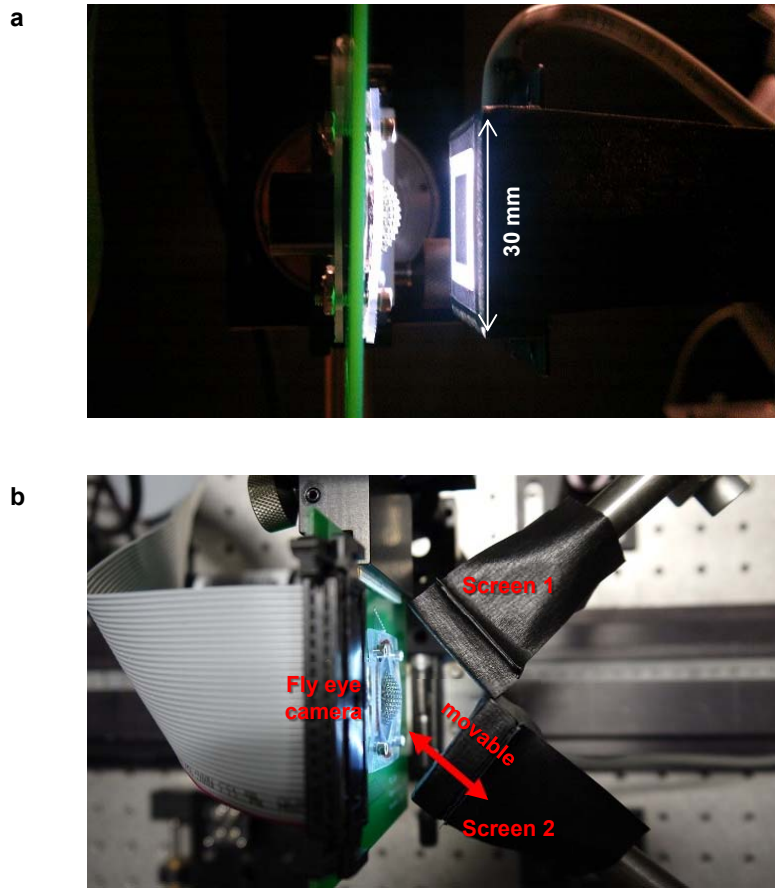


Figure S17. Photographs of the optical setup for image acquisition with (a) single and (b) double panel.

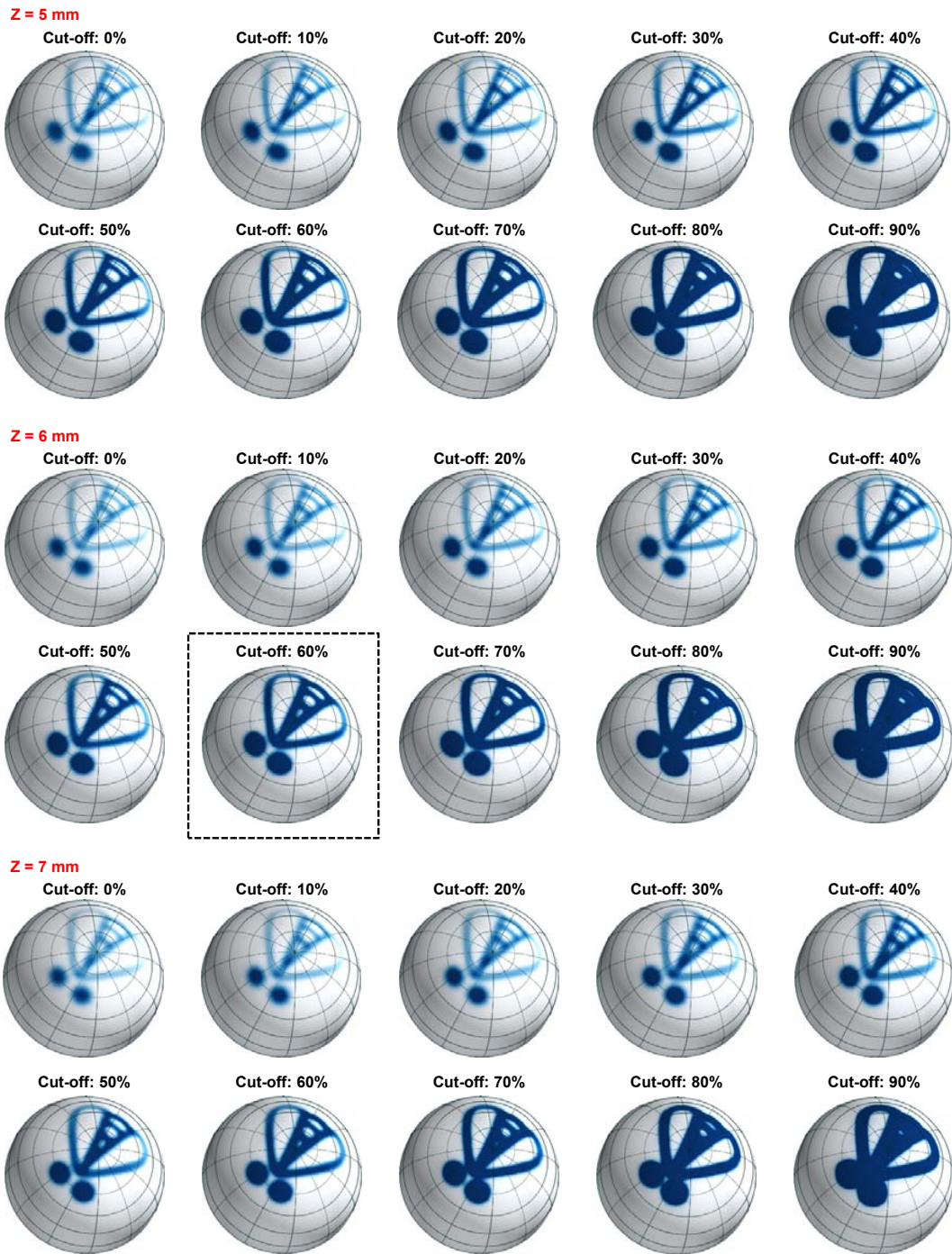


Figure S18. Images of a fly with 10 different cut-off levels computed by ray-tracing analysis at three different distances. The image in the dashed box corresponds to the left image of Fig. 3c.

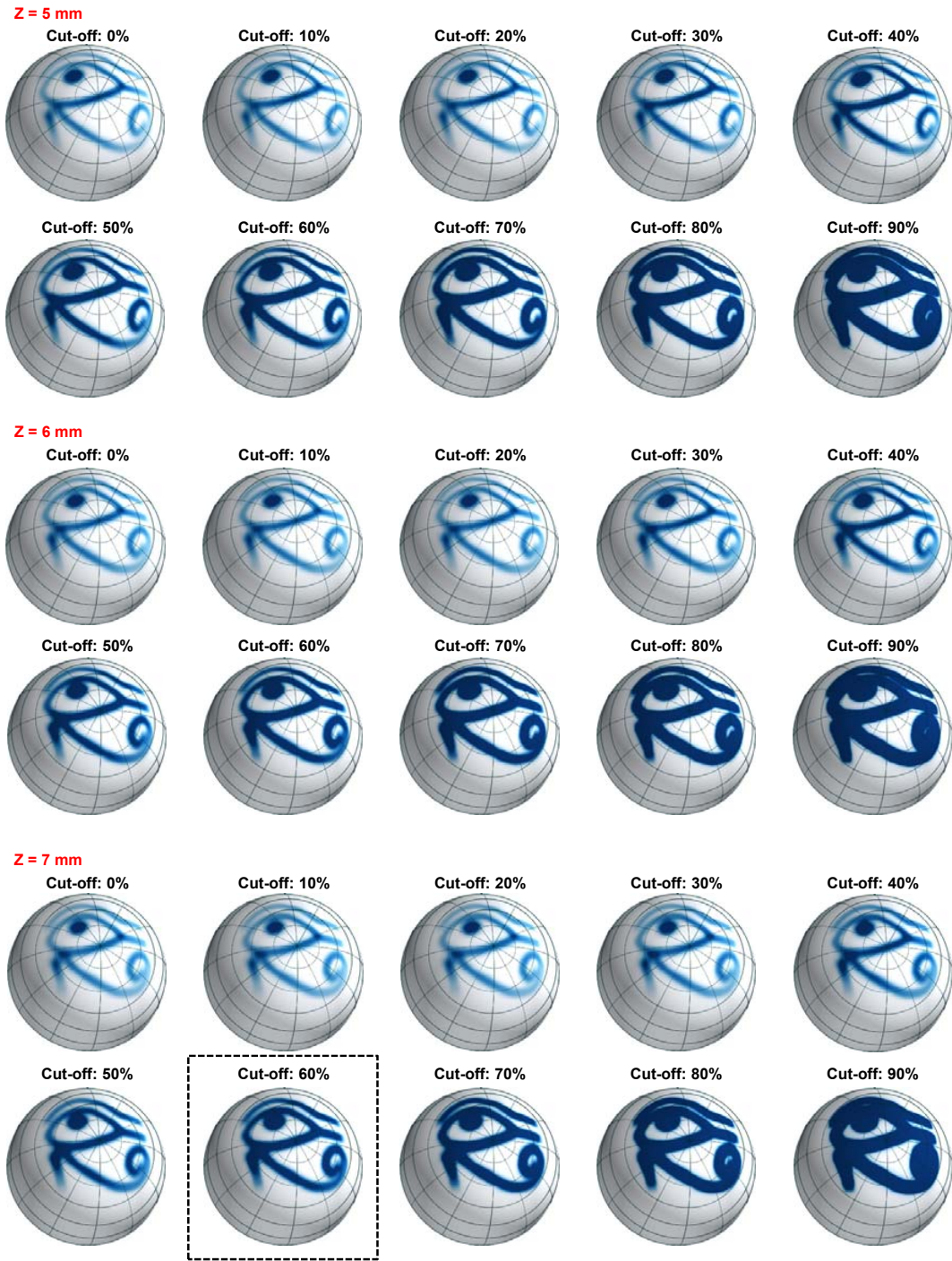


Figure S19. Images of a 'Horus eye' with 10 different cut-off levels computed by ray-tracing analysis at three different distances. The image in the dashed box corresponds to the right image of Fig. 3c.

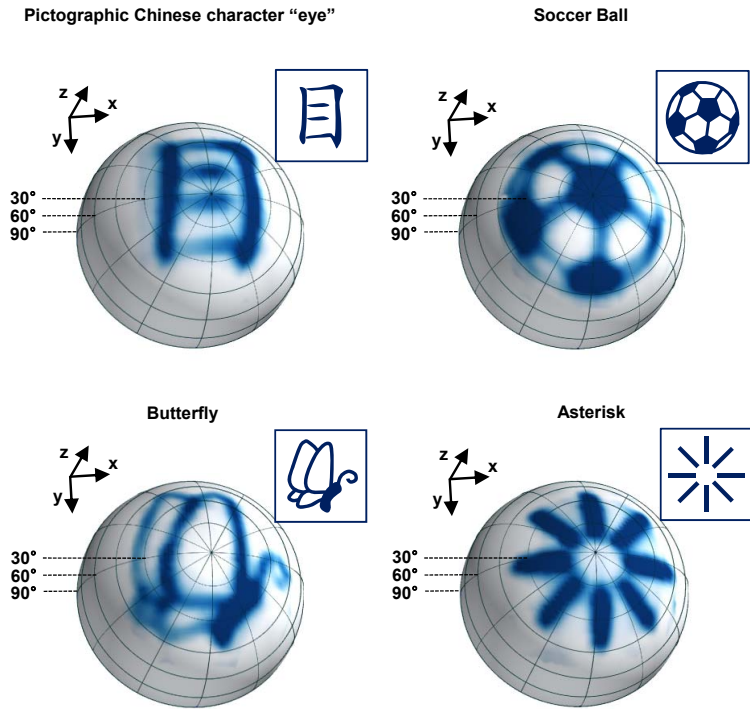


Figure S20. Representative imaging results for four different line art images captured with a hemispherical, apposition compound eye camera and rendered on a hemispherical surface that matches the shape of the device.

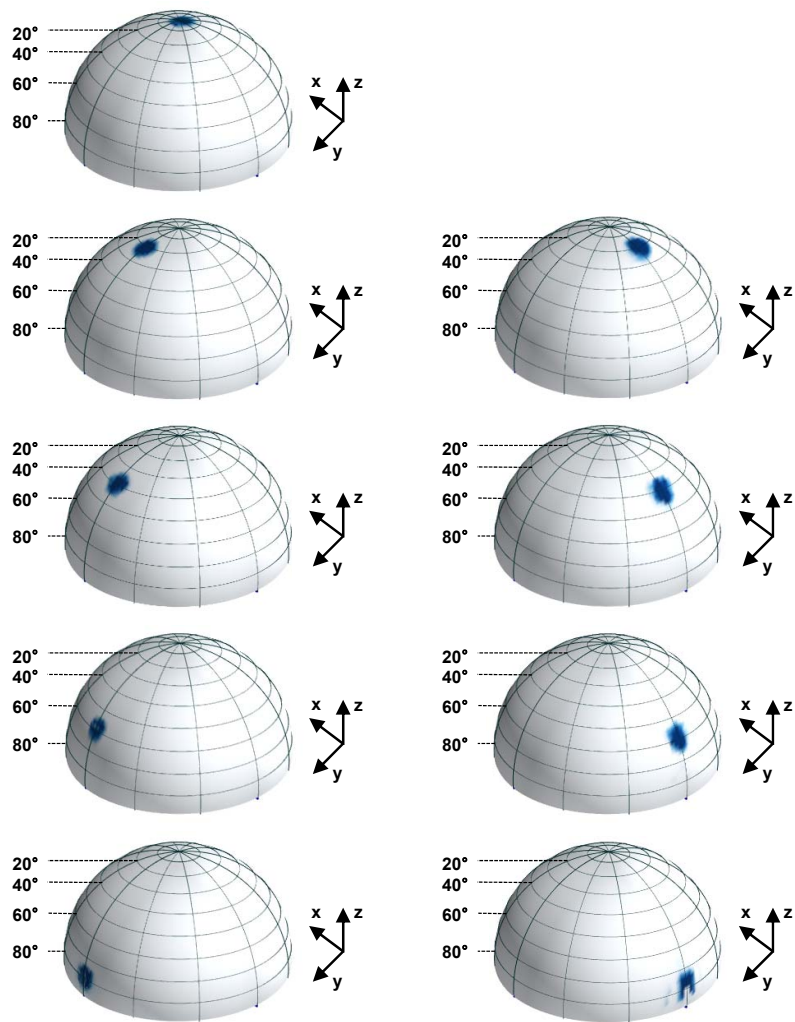


Figure S21. Images of illuminated laser spot on the camera at a nine different incident angles (from  $0^\circ$  to  $80^\circ$  in  $\theta$  direction and from  $20^\circ$  to  $80^\circ$  in  $\phi$  direction with  $20^\circ$  steps), rendered on a hemisphere surface

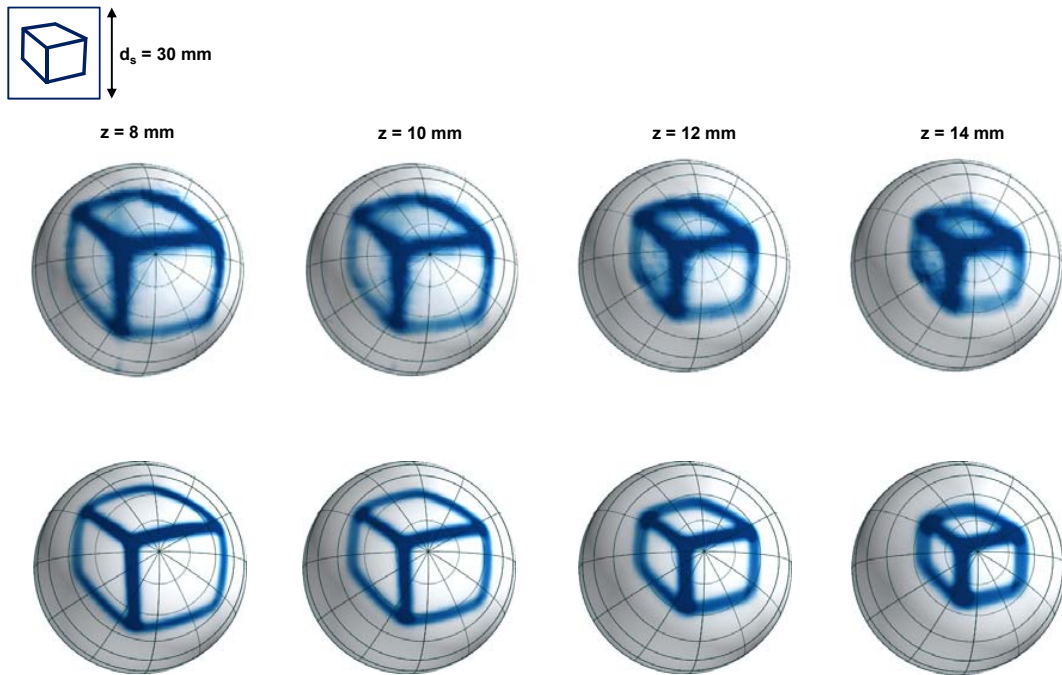


Figure S22. (top) Images of a 3D box captured at four different distances from the camera. (bottom) corresponding simulation images

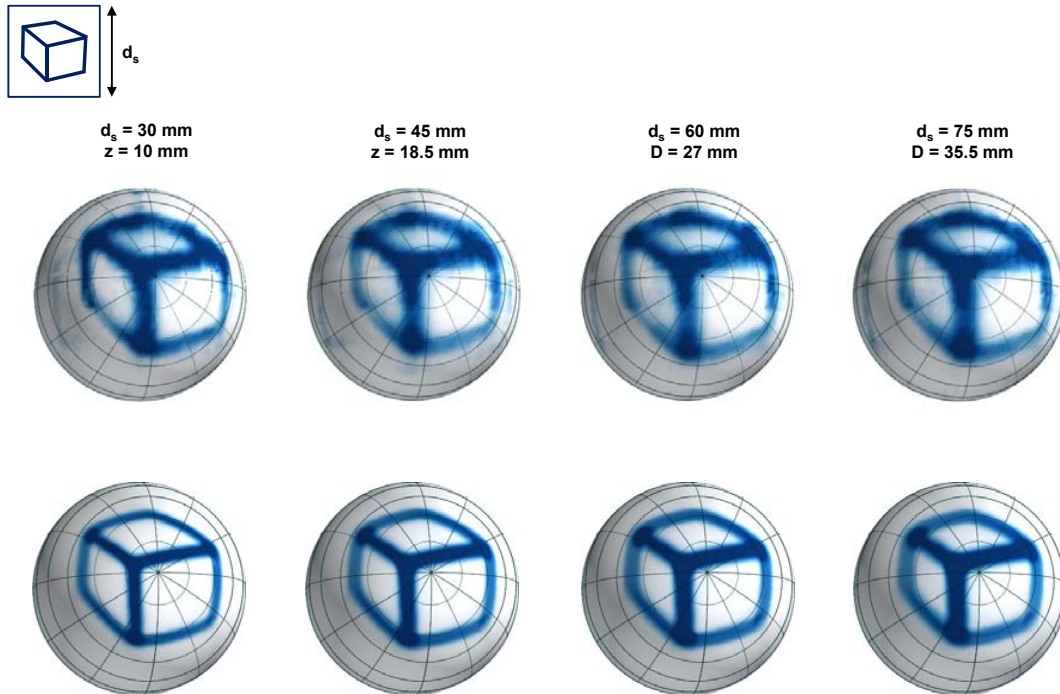


Figure S23. (top) Images of a 3D box captured at four different distances but with the same angular size. The sizes of object panels proportionally increase as the distance increases. (bottom) corresponding simulation images